

Undisturbed velocity recovery with transient and weak inertia effects in volume-filtered simulations of particle-laden flows

Fabien Evrard^{a,*}, Akshay Chandran^b, Ricardo Cortez^c, Berend van Wachem^b

^aDepartment of Aerospace Engineering, University of Illinois Urbana-Champaign, Urbana, IL 61801, United States

^bChair of Mechanical Process Engineering, Otto-von-Guericke-Universität Magdeburg, 39106 Magdeburg, Germany

^cMathematics Department, Tulane University, New Orleans, LA 70118, United States

Abstract

In volume-filtered Euler-Lagrange simulations of particle-laden flows, the fluid forces acting on a particle are estimated using reduced models, which rely on the knowledge of the local *undisturbed flow* for that particle. Since the two-way coupling between the particle and the fluid creates a local flow perturbation, the filtered fluid velocity interpolated to the particle location must be corrected prior to estimating the fluid forces, so as to subtract the contribution of this perturbation and recover the local undisturbed flow with good accuracy. In this manuscript, we present a new model for estimating a particle's self-induced flow disturbance that accounts for its transient development and for inertial effects related to finite particle Reynolds numbers. The model also does not require the direction of the momentum feedback to align with the direction of the particle's relative velocity, allowing force contributions other than the steady drag force to be considered. It is based upon the linearization of the volume-filtered equations governing the particle's self-induced flow disturbance, such that their solution can be expressed as a linear combination of regularized transient Stokeslet contributions. Tested on a range of numerical cases, the model is shown to consistently estimate the particle's self-induced flow disturbance with high accuracy both in steady and highly transient flow environments, as well as for finite particle Reynolds numbers.

© 2024. This manuscript version is made available under the CC-BY-NC-ND 4.0 license.

<http://creativecommons.org/licenses/by-nc-nd/4.0>

1. Introduction

Simulating particle-laden flows of practical interest often calls for the volume-filtering of the equations governing the fluid flow, so as to minimize the number of numerical degrees of freedom needed to reach an adequate level of accuracy. Such filtering was formalized several decades ago [1, 2], and is commonly referred to as volume-filtered Euler-Lagrange (VF-EL) or simply Euler-Lagrange (EL) modeling, when individual particles are kept track of [3–6]. In VF-EL simulations, the sub-filter scales of the flow, which typically include the details of the flow around individual particles, are not resolved and require modeling. Among the terms requiring closure is the momentum exchange between the Lagrangian particles and the Eulerian fluid. A two-way coupling indeed exists between the particles and the fluid, in which the fluid exerts a force and torque on the particles and the particles exert the opposite force and torque on the fluid [7]. Since the details of the flow around individual particles is not known in VF-EL simulations, fluid forces and torques must be estimated from the knowledge of the filtered flow using reduced models.

In the limit of vanishing Reynolds number and infinitely large flow domain, the motion of a particle immersed in a non-uniform flow is governed by the integro-differential Maxey-Riley-Gatignol (MRG) equation [8, 9]. The MRG equation is classically extended to finite Reynolds number regimes through the introduction of empirical correction factors [10–12] and lift force contributions [13]. In the MRG or extended-MRG equation, all force contributions are expressed in terms of the *undisturbed flow*, which is the conceptual modification of the particle-laden flow in which the particle under consideration is removed and replaced by fluid. The filtered flow, solution to the volume-filtered governing equations, is evidently unlike the undisturbed flow since the momentum fed back to the fluid by the particle creates a local *self-induced flow perturbation* that is not present in the undisturbed flow. The magnitude of this self-induced

*Corresponding author

Email address: fevrard@illinois.edu (Fabien Evrard)

velocity disturbance has been known to increase with the ratio $d_n/\max(\ell_{\mathcal{K}}, \ell_{\Delta x})$, where d_n is the particle diameter, $\ell_{\mathcal{K}}$ is the length-scale of the filtering kernel, if one is explicitly used, and $\ell_{\Delta x}$ is the filtering length-scale related to the discretization [14–16]. In traditional VF-EL approaches, such as the Particle-Source-In-Cell (PSI-CELL) method of Crowe et al. [17], $\ell_{\mathcal{K}} = \ell_{\Delta x}$ since the computational mesh acts as the filter. Only recently has the research community started to consider filter length-scales that are larger than that of the computational mesh, $\ell_{\mathcal{K}} > \ell_{\Delta x}$, in an effort to mitigate mesh dependency [4, 5, 18, 19].

Over the past years, the amount of scientific literature on the recovery of the undisturbed flow velocity from the knowledge of the filtered flow has significantly increased. The models that have been proposed commonly provide means to estimate the velocity disturbance induced by a particle as

$$\mathbf{u}' = \text{Model}(\bar{\mathbf{u}}, \text{Re}_\ell, \ell_{\mathcal{K}}, \ell_{\Delta x}), \quad (1)$$

where $\bar{\mathbf{u}}$ is the filtered velocity solution to the volume-filtered governing equations and Re_ℓ some definition of the Reynolds number, such that the undisturbed velocity associated with the particle can be recovered as

$$\tilde{\mathbf{u}} = \bar{\mathbf{u}} - \mathbf{u}'. \quad (2)$$

Early attempts at such modeling are based on the steady Stokes flow solution of the particle’s self-induced flow disturbance [20–22]. More recently, Gualtieri et al. [23] propose a model based on the solution of the unsteady Stokes equations with a time regularization treating singularities. Their approach is extended to wall-bounded flows in [24]. Horwitz and Mani [25, 26] propose a model approximating the particle’s self-induced velocity disturbance as a truncated power series expansion, whose coefficients are empirically fitted to data. Ireland and Desjardins [27] explicitly filter the analytical solution of the Stokes flow around a sphere to provide an approximation of the particle’s self-induced flow disturbance. Esmaily and Horwitz [28] propose a model in which a computational cell is treated as a solid object dragged at a velocity identical to that of the disturbance created by the particle. Their model is extended to wall bounded flows in [29]. Deriving an analytical closed-form expression for the central component of the regularized Oseenlet operator that is aligned with undisturbed flow, considering a Gaussian filtering kernel, Balachandar et al. [6] propose a model that accurately predicts the particle’s self-induced flow disturbance at finite Reynolds numbers. This work is extended to nonlinear regularizations by Poustis et al. [18], and to a compact polynomial filtering kernel [30] by Evrard et al. [31], based on the regularized Stokeslet operator introduced by Cortez [45]. The work of [6] is also generalized to a vector correction procedure in [32], enabling cases for which the direction of the momentum feedback need not be aligned with the relative velocity of the particle. Pakseresht and Apte [33] propose to solve an auxiliary set of governing equations that extracts all particle-induced velocity perturbations at once. Horwitz et al. [34] develop a discrete Green’s operator for the Stokes equations to provide an estimator of the particle’s self-induced flow disturbance that naturally handles boundary conditions. Finally, a correction for finite volume-fraction effects on the particle’s self-induced velocity disturbance is proposed by Kim and Balachandar [35].

Models based on steady solutions to the Stokes, Oseen, or Navier-Stokes equations [e.g., 21, 26, 27, 31, 34] can fail to meaningfully predict a particle’s self-induced flow disturbance when the time-scale associated with the particle motion is similar to, or smaller than the time-scale at which the flow disturbance develops. Among the models listed in the previous paragraph, few consider the transient evolution of the particle’s self-induced flow disturbance [6, 23, 24, 28, 29, 32, 33]. Even fewer combine this feature with the ability to consider particles moving at finite Reynolds numbers [6, 28, 29], while all relying on some form of empirical fitting. To the authors’ knowledge, no model yet presents the ability to concurrently consider transient effects, particles moving at finite Reynolds numbers, and an arbitrary orientation of the momentum feedback with respect to the relative velocity of the particle. This manuscript presents an attempt at doing so, which relies on the linearization of the equations governing the particle’s self-induced flow disturbance so as to express its velocity as a temporal and spatial convolution integral involving known analytical operators. The temporal convolution integral is approximated with what is essentially a “left-hand” integration rule, while the spatial convolution integral is estimated using pre-computed maps of the (spatially and temporally) regularized transient Stokeslet operators. The resulting model is free of heuristics and empirical coefficients, but requires seeding and keeping track of fluid tracers along the trajectory of a particle, which presents a non-negligible computational cost. The amount of tracers needing to be tracked for the model to remain accurate, however, can be kept to a minimum owing to the temporal and spatial decay of the transient Stokeslet operators.

The remainder of this manuscript is organized as follows: Section 2 introduces the volume-filtering of

the incompressible Navier-Stokes equations in the context of particle-laden flow and the terms requiring closure; Section 3 describes the proposed model for the estimation of a particle's self-induced flow disturbance, used to recover the undisturbed velocity associated with that particle; Section 4 discusses special cases for which the proposed model recovers well-known analytical solutions; Section 5 details the numerical implementation of the model and studies its spatial and temporal convergence; Section 6 presents results of VF-EL simulations that employ the proposed model, and verifies its accuracy across a wide range of flow and numerical parameters. It also discusses how to balance computational cost with the accuracy of the model. Finally, conclusions are drawn in Section 7.

2. Problem position

This section introduces the equations governing particle-laden flows and their volume-filtering. After listing the terms requiring closure, we identify the problem addressed by the model proposed in Section 3.

2.1. Governing equations of incompressible particle-laden flow

Let us consider a flow domain Ω within which N freely moving rigid particles, occupying the volumes $\Omega_n(t), n \in \{1, \dots, N\}$, are surrounded by an incompressible fluid with constant density and viscosity occupying $\Omega_f(t) = \Omega \setminus (\cup_n \Omega_n(t))$, as illustrated in Figure 1. Gravity is, for now, ignored. The equations governing the fluid motion inside $\Omega_f(t)$ are the continuity and momentum equations

$$\nabla \cdot \mathbf{u} = 0, \quad (3)$$

$$\rho \left(\frac{\partial \mathbf{u}}{\partial t} + \nabla \cdot (\mathbf{u} \otimes \mathbf{u}) \right) = -\nabla p + \mu \nabla^2 \mathbf{u}, \quad (4)$$

where \mathbf{u} is the velocity vector of the fluid, p is the pressure within the fluid, ρ is the fluid density, and μ is the dynamic fluid viscosity. At the particle surfaces, the fluid velocity, \mathbf{u} , is subject to the boundary condition

$$\mathbf{u}(\mathbf{x}, t) = \mathbf{U}_n(t) + \boldsymbol{\omega}_n(t) \times (\mathbf{x} - \mathbf{X}_n(t)), \quad \forall \mathbf{x} \in \partial\Omega_n(t), n \in \{1, \dots, N\}, \quad (5)$$

where \mathbf{X}_n , \mathbf{U}_n and $\boldsymbol{\omega}_n$ are the center of mass, translational and rotational velocities of the n^{th} particle, respectively. The equations governing the motion of the n^{th} rigid particle are

$$\frac{d\mathbf{X}_n(t)}{dt} = \mathbf{U}_n(t), \quad M_n \frac{d\mathbf{U}_n(t)}{dt} = \mathbf{F}_n(t), \quad (6)$$

$$\frac{d\boldsymbol{\theta}_n(t)}{dt} = \boldsymbol{\omega}_n(t), \quad \boldsymbol{\Lambda}_n \cdot \frac{d\boldsymbol{\omega}_n(t)}{dt} = \mathbf{T}_n(t), \quad (7)$$

where M_n is the mass of the n^{th} particle, $\boldsymbol{\Lambda}_n$ its moment of inertia tensor, and $\boldsymbol{\theta}_n$ its angular position. The vectors \mathbf{F}_n and \mathbf{T}_n correspond to the resultants of the fluid forces and torques acting on the n^{th} particle, respectively, given as

$$\mathbf{F}_n(t) = \int_{\partial\Omega_n(t)} (-p(\mathbf{x}, t)\mathbf{n} + \boldsymbol{\tau}(\mathbf{x}, t) \cdot \mathbf{n}) \, d\mathbf{x}, \quad (8)$$

and

$$\mathbf{T}_n(t) = \int_{\partial\Omega_n(t)} (-p(\mathbf{x}, t)\mathbf{n} + \boldsymbol{\tau}(\mathbf{x}, t) \cdot \mathbf{n}) \times (\mathbf{x} - \mathbf{X}_n(t)) \, d\mathbf{x}, \quad (9)$$

where \mathbf{n} is the normal to $\partial\Omega_n(t)$ pointing towards the fluid, and $\boldsymbol{\tau}$ the viscous stress tensor of the fluid. The system of all previous equations can be closed and solved numerically. However, its accurate numerical solution requires a spatial resolution that is prohibitively expensive as the number of particles becomes significant, since a minimum of 15 to 20 computational cells across each particle diameter is necessary [36]. Currently, it is possible to accurately solve such systems with up to $N \sim \mathcal{O}(10^5)$ particles [see, e.g., 37–39], leading to $\mathcal{O}(10^9)$ computational degrees of freedom per timestep. For systems with many more than $N \sim \mathcal{O}(10^5)$ particles, one must resort to solving an averaged representation of the flow, for which a much less restrictive spatial resolution can be chosen.

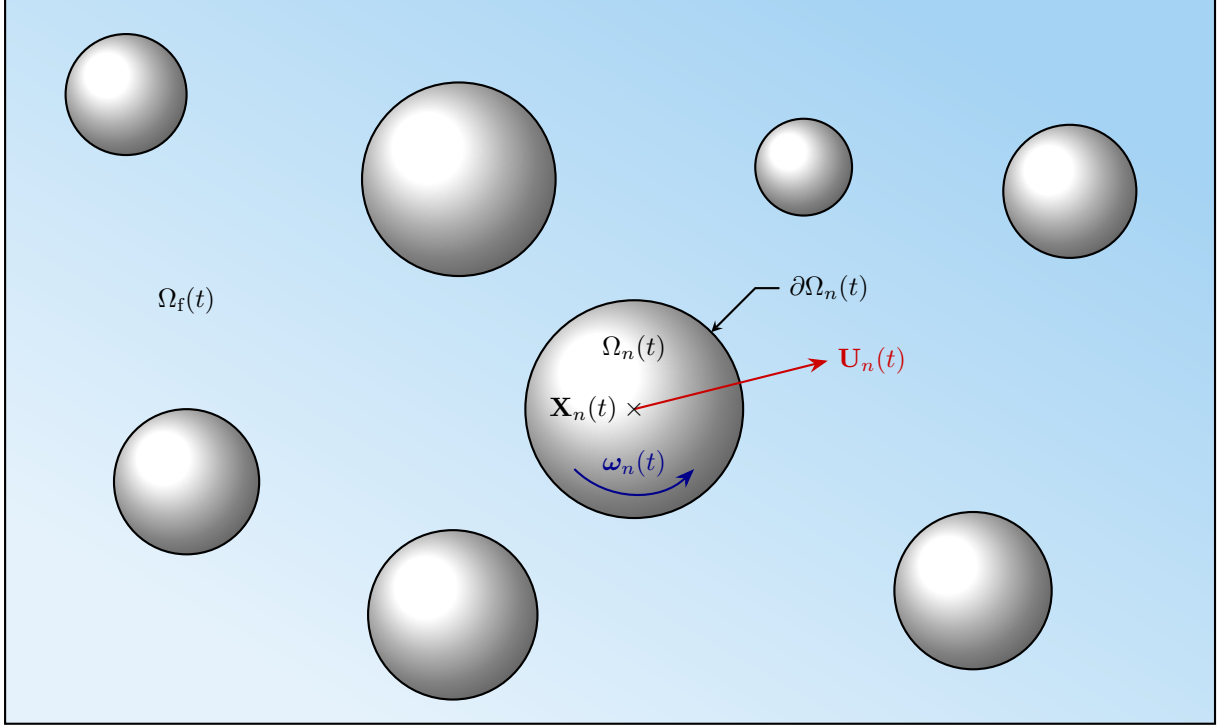


Figure 1: The flow domain Ω is the union of the domain occupied by the fluid, $\Omega_f(t)$, and that occupied by the particles, $\cup_n \Omega_n(t)$.

2.2. Volume-filtered Euler-Lagrange modeling

Volume-averaged or volume-filtered approaches are widely used for studying the behavior of particle-laden flows at the meso- or macro-scale, often referred to as volume-filtered Euler-Lagrange (VF-EL) methods [5, 6]. They rely on the spatial convolution¹ of the governing equations with a normalized radial kernel $\mathcal{K} : \mathbb{R}^+ \rightarrow \mathbb{R}^+$. In order for this kernel to be normalized, its integral over the three-dimensional real space must satisfy

$$\int_{\mathbb{R}^3} \mathcal{K}(\|\mathbf{x}\|) d\mathbf{x} = 1. \quad (10)$$

The kernel length-scale, ℓ , is defined as in [1] as the radius of the ball² \mathbb{B}_ℓ for which

$$\int_{\mathbb{B}_\ell} \mathcal{K}(\|\mathbf{x}\|) d\mathbf{x} = 4\pi \int_0^\ell r^2 \mathcal{K}(r) dr = \frac{1}{2}. \quad (11)$$

Examples of kernels that can be employed for VF-EL simulations are provided in Figure 2. The resulting volume-filtered governing equations, which are now defined on the entire domain Ω instead of being limited to the fluid domain $\Omega_f(t)$, read as [1, 5, 6]

$$\frac{\partial \varepsilon}{\partial t} + \nabla \cdot \bar{\mathbf{u}}_\varepsilon = 0, \quad (12)$$

$$\rho \left(\frac{\partial \bar{\mathbf{u}}_\varepsilon}{\partial t} + \nabla \cdot (\bar{\mathbf{u}}_\varepsilon \otimes \bar{\mathbf{u}}_\varepsilon) \right) = -\nabla \bar{p}_\varepsilon + \mu \nabla^2 \bar{\mathbf{u}}_\varepsilon + \mathbf{f} - \mathcal{U}_{\text{Re}} + \mathcal{U}_\mu. \quad (13)$$

In these volume-filtered equations:

- ε is the fluid volume fraction, defined as

$$\varepsilon = \mathcal{K} \otimes \zeta_f, \quad (14)$$

¹The spatial convolution of two scalar functions φ and ψ in \mathbb{R}^3 is given as $[\varphi \otimes \psi](\mathbf{x}, t) = \int_{\mathbb{R}^3} \varphi(\mathbf{y}, t) \psi(\mathbf{x} - \mathbf{y}, t) d\mathbf{y}$

²The ball of radius ℓ , in \mathbb{R}^3 , is the volume bounded by the sphere of radius ℓ .

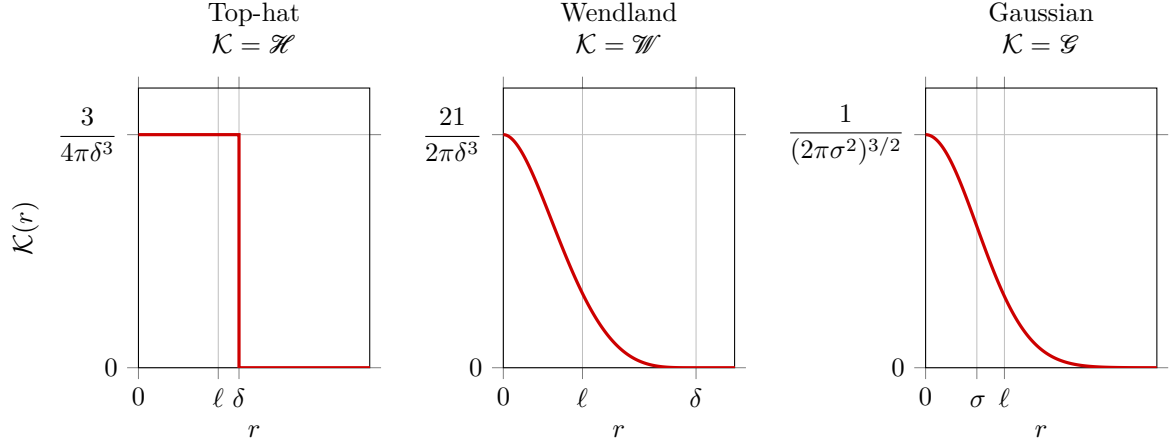


Figure 2: Examples of three convolution kernels that can be used for VF-EL simulations: the top-hat kernel \mathcal{H} , defined in Eq. (A.1), the polynomial Wendland kernel \mathcal{W} [30], defined in Eq. (A.11), and the Gaussian kernel \mathcal{G} , defined in Eq. (A.6). The kernels \mathcal{H} and \mathcal{W} are compactly supported on $[0, \delta]$, whereas \mathcal{G} is supported on \mathbb{R}^+ . Each kernel is normalised, i.e. satisfies Eq. (10). The length-scale ℓ associated with each kernel, as defined by Eq. (11), is indicated on the horizontal axes.

with ζ_f the fluid indicator function [1, 2, 40],

$$\zeta_f(\mathbf{x}, t) = \begin{cases} 1 & \mathbf{x} \in \Omega_f(t) \\ 0 & \mathbf{x} \notin \Omega_f(t) \end{cases} . \quad (15)$$

The fluid volume fraction can equivalently be written as

$$\varepsilon = 1 - \sum_{n=1}^N \varepsilon_n , \quad (16)$$

where ε_n is the volume fraction contribution of the n^{th} particle given as

$$\varepsilon_n = \mathcal{K} \circledast \zeta_n , \quad (17)$$

with ζ_n the indicator function associated with the n^{th} particle,

$$\zeta_n(\mathbf{x}, t) = \begin{cases} 1 & \mathbf{x} \in \Omega_n(t) \\ 0 & \mathbf{x} \notin \Omega_n(t) \end{cases} . \quad (18)$$

The fluid volume fraction, ε , is defined over the entire domain Ω . By construction with Eq. (14) or Eq. (16), it satisfies $0 \leq \varepsilon \leq 1$. If the radius of the kernel's support is larger than the radius of the particles, one can even write the strict inequality $0 < \varepsilon \leq 1$; a necessary condition for the volume-filtered governing equations not to become ill-posed. The convolution integral in Eq. (17) can be derived into a closed form expression for some specific kernels. Balachandar and Liu [32] have for instance shown that when \mathcal{K} is the Gaussian kernel \mathcal{G} of standard deviation σ (defined in Eq. (A.6)), the volume fraction contribution of the n^{th} particle is exactly given as

$$\begin{aligned} \varepsilon_n(\mathbf{x}, t) &= [\mathcal{G} \circledast \zeta_n](\mathbf{x}, t) \\ &= \frac{2\pi\sigma^4}{\chi_n(\mathbf{x}, t)} \left(\mathcal{G}(\chi_n(\mathbf{x}, t) + r_n) - \mathcal{G}(\chi_n(\mathbf{x}, t) - r_n) \right) \\ &\quad + \frac{1}{2} \left(\operatorname{erf} \left((\chi_n(\mathbf{x}, t) + r_n) / \sqrt{2}\sigma \right) - \operatorname{erf} \left((\chi_n(\mathbf{x}, t) - r_n) / \sqrt{2}\sigma \right) \right) \end{aligned} \quad (19)$$

$$(20)$$

with r_n the radius of the n^{th} particle, and $\chi_n(\mathbf{x}, t) = \|\mathbf{x} - \mathbf{X}_n(t)\|$ the distance to its center. In practice, ε_n is often approximated as

$$\varepsilon_n(\mathbf{x}, t) \simeq \mathcal{K}(\chi_n(\mathbf{x}, t)) V_n , \quad (21)$$

with V_n the volume of the n^{th} particle, under the assumption that the length-scale of the filter, ℓ , is

large compared to the particle radius r_n . With this approximation, ε is not bounded by construction anymore, and one must make sure that ℓ is large enough as to guarantee that $0 < \varepsilon \leq 1$ [19].

- $\bar{\mathbf{u}}_\varepsilon$ and \bar{p}_ε are the ε -weighted filtered velocity and pressure, defined as

$$\bar{\mathbf{u}}_\varepsilon = \mathcal{K} \otimes \zeta_{\mathbf{u}} = \varepsilon \bar{\mathbf{u}}, \quad (22)$$

$$\bar{p}_\varepsilon = \mathcal{K} \otimes \zeta_p = \varepsilon \bar{p}, \quad (23)$$

with

$$\zeta_{\mathbf{u}}(\mathbf{x}, t) = \begin{cases} \mathbf{u}(\mathbf{x}, t) & \mathbf{x} \in \Omega_f(t) \\ 0 & \mathbf{x} \notin \Omega_f(t) \end{cases}, \quad (24)$$

$$\zeta_p(\mathbf{x}, t) = \begin{cases} p(\mathbf{x}, t) & \mathbf{x} \in \Omega_f(t) \\ 0 & \mathbf{x} \notin \Omega_f(t) \end{cases}. \quad (25)$$

Note that these quantities, as well as the filtered velocity and pressure, $\bar{\mathbf{u}}$ and \bar{p} , are defined over the entire domain Ω .

- \mathbf{f} represents the transfer of momentum between particles and fluid given as

$$\mathbf{f}(\mathbf{x}, t) = - \sum_{n=1}^N \int_{\partial\Omega_n(t)} \mathcal{K}(\|\mathbf{x} - \mathbf{y}\|) (-p(\mathbf{y}, t)\mathbf{n} + \boldsymbol{\tau}(\mathbf{y}, t) \cdot \mathbf{n}) \, d\mathbf{y}. \quad (26)$$

It is often approximated as

$$\mathbf{f}(\mathbf{x}, t) \simeq - \sum_{n=1}^N \mathcal{K}(\|\mathbf{x} - \mathbf{X}_n(t)\|) \mathbf{F}_n(t), \quad (27)$$

where \mathbf{F}_n is the force exerted by the fluid on the n^{th} particle, previously defined in Eq. (8), although this approximation is only strictly valid for $\ell \gg r_n$ [41].

- \mathcal{Z}_{Re} is an unclosed term akin to the divergence of Reynolds stresses, given by

$$\mathcal{Z}_{\text{Re}} = \nabla \cdot (\varepsilon \overline{\mathbf{u} \otimes \mathbf{u}} - \bar{\mathbf{u}}_\varepsilon \otimes \bar{\mathbf{u}}_\varepsilon). \quad (28)$$

- \mathcal{Z}_μ an unclosed term resulting from the filtering of the viscous stresses, given by

$$\mathcal{Z}_\mu = \mu \left(\varepsilon \overline{\nabla^2 \mathbf{u}} - \nabla^2 \bar{\mathbf{u}}_\varepsilon \right). \quad (29)$$

In this new set of volume-filtered governing equations, and from now on, we neglect particle rotation. The motion of the particles is still governed by Eqs. (6), however $\mathbf{F}_n(t)$ cannot be estimated using Eq. (8) since the quantities that are solved for and known are the volume-filtered pressure and velocity, \bar{p} and $\bar{\mathbf{u}}$, in lieu of the actual pressure and velocity of the flow around the particle, p and \mathbf{u} . Reduced models must therefore be used to estimate the fluid force acting on a particle, as given for instance by the Maxey-Riley-Gatignol (MRG) equation [8, 9],

$$\begin{aligned} \mathbf{F}_n(t) = & \mathbf{F}_{n,\text{drag}}(\tilde{\mathbf{u}}_{n,\partial\Omega_n}(t), \mathbf{U}_n(t)) \\ & + \mathbf{F}_{n,\text{undist.}}(\tilde{\mathbf{u}}_{n,\Omega_n}(t)) \\ & + \mathbf{F}_{n,\text{virt.}}(\tilde{\mathbf{u}}_{n,\Omega_n}(t), \mathbf{U}_n(t)) \\ & + \mathbf{F}_{n,\text{hist.}}(\tilde{\mathbf{u}}_{n,\partial\Omega_n}(t), \mathbf{U}_n(t)). \end{aligned} \quad (30)$$

In this equation, $\mathbf{F}_{n,\text{drag}}$ is the steady viscous drag force contribution, $\mathbf{F}_{n,\text{undist.}}$ is the force contribution of the undisturbed flow stresses, $\mathbf{F}_{n,\text{virt.}}$ is the unsteady virtual mass force contribution, and $\mathbf{F}_{n,\text{hist.}}$ is the unsteady viscous history force contribution. The variable $\tilde{\mathbf{u}}_n$ corresponds to the *undisturbed fluid flow velocity for the n^{th} particle*, which is the fluid velocity as though the n^{th} particle under consideration had been taken out of the flow domain (see Figure 3).

The subscripts $\partial\Omega_n$ and Ω_n in the MRG Eq. (30) indicate that the undisturbed velocity has been averaged

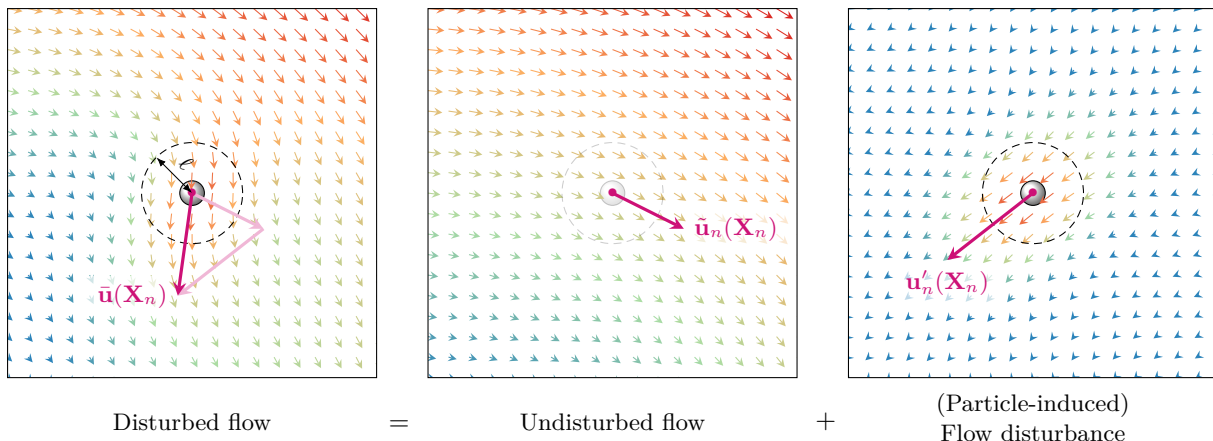


Figure 3: The velocity field solution to the volume-filtered governing equations (12) and (13) (the *disturbed flow* velocity) is equal to the sum of the *undisturbed flow* velocity for a given particle and of the *velocity disturbance* induced by that particle. The undisturbed flow velocity is needed to accurately approximate the fluid force acting on the particle using the MRG equation.

over the particle's surface and volume, respectively, i.e.,

$$\tilde{\mathbf{u}}_{n,\partial\Omega_n}(t) = \frac{1}{S_n} \int_{\partial\Omega_n(t)} \tilde{\mathbf{u}}_n(\mathbf{x}, t) \, d\mathbf{x}, \quad (31)$$

$$\tilde{\mathbf{u}}_{n,\Omega_n}(t) = \frac{1}{V_n} \int_{\Omega_n(t)} \tilde{\mathbf{u}}_n(\mathbf{x}, t) \, d\mathbf{x}, \quad (32)$$

where S_n and V_n are the surface area and volume of the n^{th} particle. Assuming spherical particles and from the Taylor series expansion of the undisturbed velocity field inside Ω_n , these averaged quantities can be approximated as [42]

$$\tilde{\mathbf{u}}_{n,\partial\Omega_n}(t) \simeq \tilde{\mathbf{u}}_n(\mathbf{X}_n(t), t) + \frac{r_n^2}{6} \nabla^2 \tilde{\mathbf{u}}_n(\mathbf{X}_n(t), t), \quad (33)$$

$$\tilde{\mathbf{u}}_{n,\Omega_n}(t) \simeq \tilde{\mathbf{u}}_n(\mathbf{X}_n(t), t) + \frac{r_n^2}{10} \nabla^2 \tilde{\mathbf{u}}_n(\mathbf{X}_n(t), t). \quad (34)$$

2.3. Objectives of this manuscript

In order to make rigorous and optimal use of the volume-filtered Euler-Lagrange method, one must:

1. Close the terms \mathcal{U}_{Re} and \mathcal{U}_μ ;
2. Close the momentum transfer term \mathbf{f} , which requires to estimate the undisturbed fluid velocity $\tilde{\mathbf{u}}$ and its Laplacian $\nabla^2 \tilde{\mathbf{u}}$ at the location of each particle from the knowledge of the filtered flow variables.

In this manuscript, we shall focus on addressing the second of these two tasks, particularly focusing on recovering an accurate undisturbed velocity from the filtered flow. To that end, we propose a new model for estimating the velocity disturbance induced by the n^{th} particle, \mathbf{u}'_n , such that its undisturbed velocity can be recovered as $\tilde{\mathbf{u}}_n = \tilde{\mathbf{u}} - \mathbf{u}'_n$. For insights on how to close the term \mathcal{U}_{Re} , an analytical closure for the term \mathcal{U}_μ , as well as a discussion on the regularization of the momentum exchange term \mathbf{f} , we refer the reader to the recent work of Hausmann et al. [41].

3. Model description

In this section, a model for recovering the undisturbed flow velocity and its Laplacian at the location of each particle is derived in the context of volume-filtered Euler-Lagrange modeling. This model relies on the linearization of the equations governing a particle's self-induced flow disturbance, which are solved using Green's functions for the resulting linear operators and discretizing the corresponding convolution integrals.

3.1. Linearized governing equations of the particle's self-induced flow disturbance

Let us consider the n^{th} particle of our ensemble of N particles, and rewrite the volume-filtered governing equations of the flow in the frame of reference of this particle. The position vector, in this frame of reference, is expressed as

$$\mathbf{y} = \mathbf{x} - \mathbf{X}_n(t), \quad (35)$$

i.e., relative to the center of the n^{th} particle. Moreover, we neglect the unclosed terms \mathcal{U}_{Re} and \mathcal{U}_{μ} . The resulting volume-filtered governing equations read as

$$\frac{\partial \varepsilon}{\partial t} + \nabla \cdot \bar{\mathbf{v}}_{\varepsilon} = 0, \quad (36)$$

$$\rho \left(\frac{\partial \bar{\mathbf{v}}_{\varepsilon}}{\partial t} + \nabla \cdot (\bar{\mathbf{v}}_{\varepsilon} \otimes \bar{\mathbf{v}}_{\varepsilon}) \right) = -\frac{d\mathbf{U}_n}{dt} - \nabla \bar{p}_{\varepsilon} + \mu \nabla^2 \bar{\mathbf{v}}_{\varepsilon} - \sum_{m=1}^N \mathcal{K}(\|\mathbf{y} - (\mathbf{X}_m - \mathbf{X}_n)\|) \mathbf{F}_m, \quad (37)$$

where $\bar{\mathbf{v}}_{\varepsilon}$ is the ε -weighted filtered fluid velocity relative to that of the n^{th} particle,

$$\bar{\mathbf{v}}_{\varepsilon}(\mathbf{y}, t) = \bar{\mathbf{u}}_{\varepsilon}(\mathbf{x}, t) - \mathbf{U}_n(t). \quad (38)$$

The undisturbed flow for the n^{th} particle is the conceptual flow in which the n^{th} particle has been removed from the flow domain. The volume-filtered equations governing this undisturbed flow thus are

$$\frac{\partial (\varepsilon + \varepsilon_n)}{\partial t} + \nabla \cdot \tilde{\mathbf{v}}_{n,\varepsilon} = 0, \quad (39)$$

$$\rho \left(\frac{\partial \tilde{\mathbf{v}}_{n,\varepsilon}}{\partial t} + \nabla \cdot (\tilde{\mathbf{v}}_{n,\varepsilon} \otimes \tilde{\mathbf{v}}_{n,\varepsilon}) \right) = -\frac{d\mathbf{U}_n}{dt} - \nabla \tilde{p}_{n,\varepsilon} + \mu \nabla^2 \tilde{\mathbf{v}}_{n,\varepsilon} + \mathcal{K}(\|\mathbf{y}\|) \mathbf{F}_n - \sum_{m=1}^N \mathcal{K}(\|\mathbf{y} - (\mathbf{X}_m - \mathbf{X}_n)\|) \mathbf{F}_m, \quad (40)$$

where $\varepsilon_n = \mathcal{G} \otimes \zeta_n$ is the volume fraction contribution of the n^{th} particle, introduced in Eq. (17) and satisfying $0 \leq \varepsilon_n \leq 1 - \varepsilon$. The quantity $\tilde{\mathbf{v}}_{n,\varepsilon} = (\varepsilon + \varepsilon_n) \tilde{\mathbf{v}}_n$ is the ε -weighted filtered undisturbed velocity, whereas $\tilde{\mathbf{v}}_n$ is the filtered undisturbed velocity for the n^{th} particle. Note that in the case of an isolated particle situated far away from other particles, $\varepsilon + \varepsilon_n \simeq 1$ and therefore $\tilde{\mathbf{v}}_n \simeq \tilde{\mathbf{v}}_{n,\varepsilon}$ locally. We now define the ε -weighted filtered velocity disturbance induced by the n^{th} particle as

$$\mathbf{v}'_{n,\varepsilon} = \bar{\mathbf{v}}_{\varepsilon} - \tilde{\mathbf{v}}_{n,\varepsilon}. \quad (41)$$

Note that since $\bar{\mathbf{v}}_{\varepsilon}$ and $\tilde{\mathbf{v}}_{n,\varepsilon}$ are both expressed relatively to the velocity of the n^{th} particle, then

$$\begin{aligned} \mathbf{v}'_{n,\varepsilon}(\mathbf{y}, t) &= \bar{\mathbf{v}}_{\varepsilon}(\mathbf{y}, t) - \tilde{\mathbf{v}}_{n,\varepsilon}(\mathbf{y}, t) \\ &= \bar{\mathbf{v}}_{\varepsilon}(\mathbf{y}, t) + \mathbf{U}_n(t) - (\tilde{\mathbf{v}}_{n,\varepsilon}(\mathbf{y}, t) + \mathbf{U}_n(t)) \\ &= \bar{\mathbf{u}}_{\varepsilon}(\mathbf{x}, t) - \tilde{\mathbf{u}}_{n,\varepsilon}(\mathbf{x}, t) \\ &= \mathbf{u}'_{n,\varepsilon}(\mathbf{x}, t). \end{aligned} \quad (42)$$

Subtracting the volume-filtered governing equations of the undisturbed flow, Eqs. (39) and (40), from those of the disturbed flow, Eqs. (36) and (37), we obtain governing equations for the ε -weighted velocity and pressure disturbances,

$$-\frac{\partial \varepsilon_n}{\partial t} + \nabla \cdot \mathbf{v}'_{n,\varepsilon} = 0, \quad (43)$$

$$\rho \left(\frac{\partial \mathbf{v}'_{n,\varepsilon}}{\partial t} + \nabla \cdot (\tilde{\mathbf{v}}_{n,\varepsilon} \otimes \mathbf{v}'_{n,\varepsilon} + \mathbf{v}'_{n,\varepsilon} \otimes \bar{\mathbf{v}}_{\varepsilon}) \right) = -\nabla p'_{n,\varepsilon} + \mu \nabla^2 \mathbf{v}'_{n,\varepsilon} - \mathcal{K}(\|\mathbf{y}\|) \mathbf{F}_n. \quad (44)$$

Since we are in the frame of reference of the n^{th} particle, $\partial\varepsilon_n/\partial t \equiv 0$, so the equations simplify to

$$\nabla \cdot \mathbf{v}'_{n,\varepsilon} = 0, \quad (45)$$

$$\rho \left(\frac{\partial \mathbf{v}'_{n,\varepsilon}}{\partial t} + \tilde{\mathbf{v}}_{n,\varepsilon} \cdot \nabla \mathbf{v}'_{n,\varepsilon} + \mathbf{v}'_{n,\varepsilon} (\nabla \cdot \tilde{\mathbf{v}}_{n,\varepsilon}) + \mathbf{v}'_{n,\varepsilon} \cdot \nabla \tilde{\mathbf{v}}_{n,\varepsilon} \right) = -\nabla p'_{n,\varepsilon} + \mu \nabla^2 \mathbf{v}'_{n,\varepsilon} - \mathcal{K}(\|\mathbf{y}\|) \mathbf{F}_n. \quad (46)$$

We further simplify these equations by neglecting the last two advection terms on the left-hand side of Eq. (46), assuming that the Reynolds number associated with the velocity disturbance is vanishingly small, i.e., $\rho\ell\|\mathbf{v}'\|/\mu \ll 1$. The resulting approximate governing equations of the particle-induced flow disturbance, in the frame of reference of the n^{th} particle, are linear and read as

$$\nabla \cdot \mathbf{v}'_{n,\varepsilon} = 0, \quad (47)$$

$$\rho \left(\frac{\partial \mathbf{v}'_{n,\varepsilon}}{\partial t} + \tilde{\mathbf{v}}_{n,\varepsilon} \cdot \nabla \mathbf{v}'_{n,\varepsilon} \right) = -\nabla p'_{n,\varepsilon} + \mu \nabla^2 \mathbf{v}'_{n,\varepsilon} - \mathcal{K}(\|\mathbf{y}\|) \mathbf{F}_n. \quad (48)$$

Finally, in order to derive an approximate analytical solution to this system of equations, we assume that $\tilde{\mathbf{v}}_{n,\varepsilon}$ varies little over the length-scales associated with the particle-induced flow disturbance. We can then consider that $\tilde{\mathbf{v}}_{n,\varepsilon}(\mathbf{y}, t) \simeq \tilde{\mathbf{V}}_{n,\varepsilon}(t)$ in the relative vicinity of $\mathbf{y} = \mathbf{0}$. In any new coordinate system centered around $\tilde{\mathbf{Y}}_n(t)$, solution to

$$\frac{d\tilde{\mathbf{Y}}_n(t)}{dt} = \tilde{\mathbf{V}}_{n,\varepsilon}(t), \quad (49)$$

and subject to some initial conditions (that we do not yet specify), the position vector reads as

$$\mathbf{z} = \mathbf{y} - \tilde{\mathbf{Y}}_n(t), \quad (50)$$

and we can rewrite the volume-filtered governing equations of the undisturbed flow as

$$\nabla \cdot \mathbf{w}'_{n,\varepsilon} = 0, \quad (51)$$

$$\rho \frac{\partial \mathbf{w}'_{n,\varepsilon}}{\partial t} = -\frac{d\tilde{\mathbf{V}}_{n,\varepsilon}}{dt} - \nabla p'_{n,\varepsilon} + \mu \nabla^2 \mathbf{w}'_{n,\varepsilon} - \mathcal{K}(\|\mathbf{z} + \tilde{\mathbf{Y}}_n\|) \mathbf{F}_n, \quad (52)$$

with $\mathbf{w}'_{n,\varepsilon}(\mathbf{z}, t) = \mathbf{v}'_{n,\varepsilon}(\mathbf{y}, t) = \mathbf{u}'_{n,\varepsilon}(\mathbf{x}, t)$. We further choose to neglect the acceleration of this coordinate system, effectively approximating $\mathbf{w}'_{n,\varepsilon}$ as the solution to the unsteady Stokes equations

$$\nabla \cdot \mathbf{w}'_{n,\varepsilon} = 0, \quad (53)$$

$$\rho \frac{\partial \mathbf{w}'_{n,\varepsilon}}{\partial t} = -\nabla p'_{n,\varepsilon} + \mu \nabla^2 \mathbf{w}'_{n,\varepsilon} - \mathcal{K}(\|\mathbf{z} + \tilde{\mathbf{Y}}_n\|) \mathbf{F}_n. \quad (54)$$

Although it might seem that we have made a lot of stringent assumptions to reach the system of equations (53)–(54), we shall see that its solution does a remarkably good job at approximating the transient evolution of the self-induced particle disturbance, even at finite particle Reynolds numbers.

3.2. Green's function for the unsteady Stokes equations

Green's function for the set of linear equations (53) and (54) is classically referred to as the *transient Stokeslet* operator and given as [43]

$$\mathfrak{J}(\mathbf{x}, t) = \frac{1}{\mu} (\mathcal{I}\nabla^2 - \nabla\nabla) b(\|\mathbf{x}\|, t), \quad (55)$$

where

$$b(r, t) = \frac{1}{8\pi} \left[\sqrt{\frac{4\nu}{\pi t}} - \frac{2\nu}{r} \operatorname{erf} \left(\frac{r}{\sqrt{4\nu t}} \right) \right], \quad (56)$$

and with $\nu = \mu/\rho$ the kinematic viscosity of the fluid. Owing to the radial symmetry of b , Eq. (55) also reads as

$$\mathfrak{J}(\mathbf{x}, t) = \frac{1}{\mu} (\mathcal{I}h_1(\|\mathbf{x}\|, t) + (\mathbf{x} \otimes \mathbf{x}) h_2(\|\mathbf{x}\|, t)), \quad (57)$$

where

$$h_1(r, t) = \frac{1}{8\pi r} \left[\frac{r^2 + 2\nu t}{rt\sqrt{\pi\nu t}} \exp\left(-\frac{r^2}{4\nu t}\right) - \frac{2\nu}{r^2} \operatorname{erf}\left(\frac{r}{\sqrt{4\nu t}}\right) \right], \quad (58)$$

$$h_2(r, t) = \frac{1}{8\pi r^3} \left[-\frac{r^2 + 6\nu t}{rt\sqrt{\pi\nu t}} \exp\left(-\frac{r^2}{4\nu t}\right) + \frac{6\nu}{r^2} \operatorname{erf}\left(\frac{r}{\sqrt{4\nu t}}\right) \right]. \quad (59)$$

The functions h_1 and h_2 are singular both in space, at $r = \|\mathbf{x}\| = 0$, and in time, at $t = 0$. The tensorial operator \mathfrak{J} governs the flow response to a point-force impulse in the Stokes regime.

3.3. Approximate solution of the particle's self-induced velocity disturbance

The solution to Eqs. (53) and (54) can be obtained analytically via convolution in space and time of the Green's function given in Eq. (57) with the regularized momentum source in Eq. (54), leading to

$$\mathbf{w}'_{n,\varepsilon}(\mathbf{z}, t) = \int_{\mathbb{R}^3} \int_0^t -\mathcal{K}(\|\mathbf{r} + \tilde{\mathbf{Y}}_n(\tau)\|) \mathbf{F}_n(\tau) \cdot \mathfrak{J}(\mathbf{z} - \mathbf{r}, t - \tau) d\tau d\mathbf{r}. \quad (60)$$

Note that, in this equation, \mathbf{r} and τ are spatial and temporal integration variables, respectively. From the definition of the previously introduced coordinate change, we know that

$$\mathbf{w}'_{n,\varepsilon}(\mathbf{z}, t) = \mathbf{w}'_{n,\varepsilon}(\mathbf{y} - \tilde{\mathbf{Y}}_n(t), t) = \mathbf{v}'_{n,\varepsilon}(\mathbf{y}, t), \quad (61)$$

therefore

$$\mathbf{v}'_{n,\varepsilon}(\mathbf{y}, t) = \int_{\mathbb{R}^3} \int_0^t -\mathcal{K}(\|\mathbf{r} + \tilde{\mathbf{Y}}_n(\tau)\|) \mathbf{F}_n(\tau) \cdot \mathfrak{J}(\mathbf{y} - \tilde{\mathbf{Y}}_n(t) - \mathbf{r}, t - \tau) d\tau d\mathbf{r}. \quad (62)$$

With the variable change $\mathbf{q} = \mathbf{r} + \tilde{\mathbf{Y}}_n(t)$, this result also reads as

$$\mathbf{v}'_{n,\varepsilon}(\mathbf{y}, t) = \int_{\mathbb{R}^3} \int_0^t -\mathcal{K}(\|\mathbf{q} - (\tilde{\mathbf{Y}}_n(t) - \tilde{\mathbf{Y}}_n(\tau))\|) \mathbf{F}_n(\tau) \cdot \mathfrak{J}(\mathbf{y} - \mathbf{q}, t - \tau) d\tau d\mathbf{q}. \quad (63)$$

Consistently with the time discretization of the volume-filtered governing equations, we can split $[0, t]$ into K time intervals $[t^{(k)}, t^{(k+1)}]$ and produce the following first-order approximation of the previous integral

$$\mathbf{v}'_{n,\varepsilon}(\mathbf{y}, t) = \sum_{k=1}^K \int_{\mathbb{R}^3} \left[\mathcal{K}(\|\mathbf{q} - (t - t^{(k)})\tilde{\mathbf{v}}_{n,\varepsilon}\|) \mathbf{F}_n(t^{(k)}) \cdot \int_{t^{(k+1)}}^{t^{(k)}} \mathfrak{J}(\mathbf{y} - \mathbf{q}, t - \tau) d\tau \right] d\mathbf{q}. \quad (64)$$

The time integral in Eq. (64) can now be derived analytically. Integrating the transient Stokeslet operator from 0 to t , we indeed obtain the persistent transient Stokeslet operator

$$\mathfrak{S}(\mathbf{x}, t) = \int_0^t \mathfrak{J}(\mathbf{x}, s) ds = \frac{1}{\mu} (\mathcal{I}\mathcal{H}_1(\|\mathbf{x}\|, t) + (\mathbf{x} \otimes \mathbf{x}) \mathcal{H}_2(\|\mathbf{x}\|, t)), \quad (65)$$

with

$$\mathcal{H}_1(r, t) = \int_0^t h_1(r, s) ds = \frac{1}{8\pi r} \left[1 + \frac{2}{r} \sqrt{\frac{\nu t}{\pi}} \exp\left(-\frac{r^2}{4\nu t}\right) - \left(1 + \frac{2\nu t}{r^2}\right) \operatorname{erf}\left(\frac{r}{\sqrt{4\nu t}}\right) \right], \quad (66)$$

$$\mathcal{H}_2(r, t) = \int_0^t h_2(r, s) ds = \frac{1}{8\pi r^3} \left[1 - \frac{6}{r} \sqrt{\frac{\nu t}{\pi}} \exp\left(-\frac{r^2}{4\nu t}\right) - \left(1 - \frac{6\nu t}{r^2}\right) \operatorname{erf}\left(\frac{r}{\sqrt{4\nu t}}\right) \right]. \quad (67)$$

Note that \mathcal{H}_1 and \mathcal{H}_2 are only singular in space at $r = \|\mathbf{x}\| = 0$.

The ε -weighted velocity disturbance, $\mathbf{v}'_{n,\varepsilon}$, can thus be approximated as

$$\mathbf{v}'_{n,\varepsilon}(\mathbf{y}, t) = \sum_{k=1}^K \mathbf{F}_n(t^{(k)}) \cdot \left[\int_{\mathbb{R}^3} \mathcal{K}(\|\mathbf{q} - (t - t^{(k)})\tilde{\mathbf{v}}_{n,\varepsilon}\|) \mathfrak{S}(\mathbf{y} - \mathbf{q}, t - \tau) d\mathbf{q} \right]_{\tau=t^{(k+1)}}^{\tau=t^{(k)}}. \quad (68)$$

The integral in Eq. (68) corresponds to the spatial convolution of \mathfrak{S} , Green's function for the Stokes flow induced by a time-persistent point-source, with the filtering kernel \mathcal{K} centered at the location

$(t - t^{(k)})\tilde{\mathbf{v}}_{n,\varepsilon}$. Let us then introduce $\mathcal{S}_{\mathcal{K}}$, Green's function for the Stokes flow induced by a time-persistent point-source regularized with the kernel \mathcal{K} ,

$$\mathcal{S}_{\mathcal{K}} = \mathcal{K} \otimes \mathcal{S}. \quad (69)$$

We also introduce $\tilde{\mathbf{Y}}_{n,k}$, the solution to the transport equation

$$\frac{d\tilde{\mathbf{Y}}_{n,k}(s)}{ds} = \tilde{\mathbf{v}}_{n,\varepsilon}(\tilde{\mathbf{Y}}_{n,k}(s), t^{(k)} + s), \quad (70)$$

subject to the initial condition $\tilde{\mathbf{Y}}_{n,k}(0) = \mathbf{0}$. The ε -weighted velocity disturbance then reads as

$$\mathbf{v}'_{n,\varepsilon}(\mathbf{y}, t) = \sum_{k=1}^K \mathbf{F}_n(t^{(k)}) \cdot \left[\mathcal{S}_{\mathcal{K}} \left(\mathbf{y} - \tilde{\mathbf{Y}}_{n,k}(t - t^{(k)}), t - \tau \right) \right]_{\tau=t^{(k+1)}}^{\tau=t^{(k)}}. \quad (71)$$

Moving back to the original canonical frame of reference, it follows that

$$\mathbf{u}'_{n,\varepsilon}(\mathbf{x}, t) = \sum_{k=1}^K \mathbf{F}_n(t^{(k)}) \cdot \left[\mathcal{S}_{\mathcal{K}} \left(\mathbf{x} - \tilde{\mathbf{X}}_{n,k}(t - t^{(k)}), t - \tau \right) \right]_{\tau=t^{(k+1)}}^{\tau=t^{(k)}}, \quad (72)$$

where $\tilde{\mathbf{X}}_{n,k}$ is the solution to

$$\frac{d\tilde{\mathbf{X}}_{n,k}(s)}{ds} = \tilde{\mathbf{u}}_{n,\varepsilon}(\tilde{\mathbf{X}}_{n,k}(s), t^{(k)} + s), \quad (73)$$

subject to the initial condition $\tilde{\mathbf{X}}_{n,k}(0) = \mathbf{X}_n(t^{(k)})$.

In practice, this means that:

- The velocity disturbance induced by a particle is a function of all previous discrete instances of the feedback force associated with that particle (i.e., it is function of $\mathbf{F}_n(t^{(k)})$, $k \in \{1, \dots, K\}$).
- Each of the discrete force instances $\mathbf{F}_n(t^{(k)})$ contributes to $\mathbf{u}'_{n,\varepsilon}$ in the form of a regularized transient Stokeslet “active” between $t^{(k)}$ and $t^{(k+1)}$, obtained via the multiplication of $\mathbf{F}_n(t^{(k)})$ with the tensorial Green's function operator $\mathcal{S}_{\mathcal{K}}$.
- Each of these regularized transient Stokeslet contributions originates from a source-location $\tilde{\mathbf{X}}_{n,k}$ advected with the undisturbed flow from $t^{(k)}$ onwards, where $t^{(k)}$ is the time of introduction of the discrete feedback force.

The discrete setup of this model is illustrated in Figure 4. Note that estimating the undisturbed velocity at each source-location $\tilde{\mathbf{X}}_{n,k}$ for its advection with Eq. (73) is tedious, complex to implement, and computationally expensive. Instead, in practice, we advect these sources with the filtered velocity, $\tilde{\mathbf{u}}_{n,\varepsilon}$, rather than the undisturbed velocity, $\tilde{\mathbf{u}}_{n,\varepsilon}$. We have found this to have little effect on the accuracy of the model, while significantly reducing its complexity and computational cost.

3.4. Approximating the Laplacian of the particles' self-induced velocity disturbance

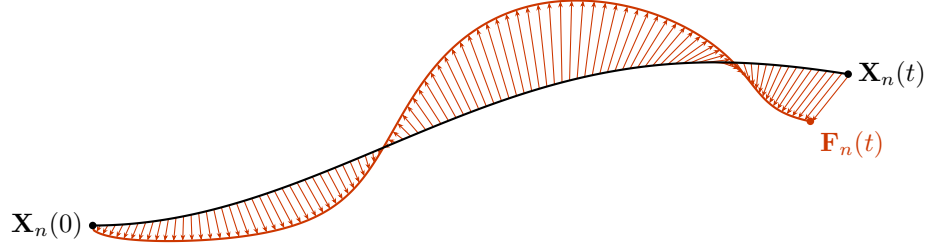
Applying the Laplacian operator to the expression in Eq. (57), it is straightforward to obtain Green's function for the Laplacian of the transient Stokeslet, also referred to as the transient potential dipole,

$$\mathcal{L}(\mathbf{x}, t) = \frac{1}{\mu} (\mathcal{I}d_1(\|\mathbf{x}\|, t) + (\mathbf{x} \otimes \mathbf{x}) d_2(\|\mathbf{x}\|, t)), \quad (74)$$

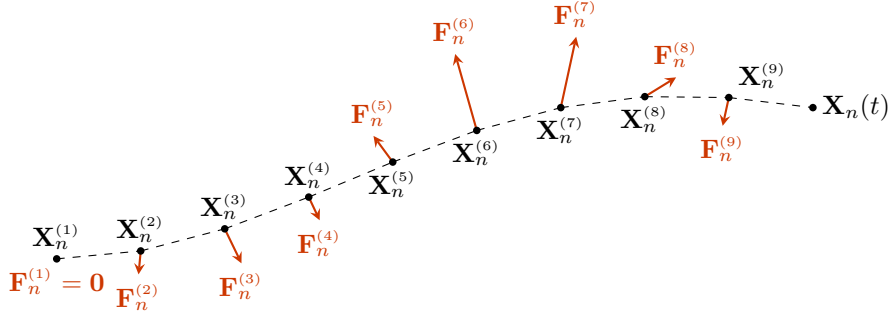
where

$$d_1(r, t) = \frac{1}{4\pi r^3} \left[\frac{(r^2 - 4\nu t) r^3}{8\nu^2 t^3 \sqrt{\pi\nu t}} \exp\left(-\frac{r^2}{4\nu t}\right) \right], \quad (75)$$

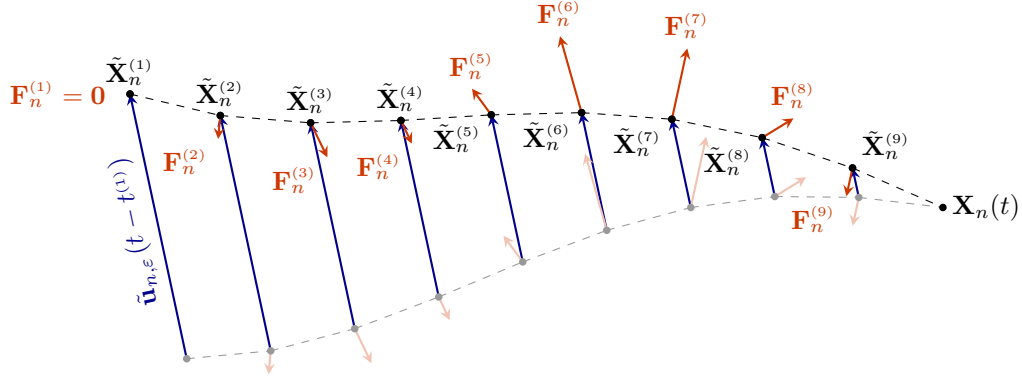
$$d_2(r, t) = \frac{-3}{4\pi r^5} \left[\frac{r^5}{24\nu^2 t^3 \sqrt{\pi\nu t}} \exp\left(-\frac{r^2}{4\nu t}\right) \right]. \quad (76)$$



(a) The n^{th} particle follows a trajectory $\mathbf{X}_n(t)$ from 0 to t , while feeding the force $-\mathbf{F}_n(t)$ back to the fluid



(b) The time interval $[0, t]$ is split into $K = 9$ intervals $[t^{(k)}, t^{(k+1)}]$ with $t^{(1)} = 0, t^{(10)} = t$. The discrete particle positions and feedback forces at the times $t^{(k)}$ are identified as $\mathbf{X}_n^{(k)} = \mathbf{X}_n(t^{(k)})$ and $-\mathbf{F}_n^{(k)} = -\mathbf{F}_n(t^{(k)})$.



(c) In accordance with the model proposed in Eq. (72), the center of each transient Stokeslet contribution needs to be transported by the undisturbed flow, from its time of injection onwards. These advected source locations, solution to Eq. (73), are identified as $\tilde{\mathbf{X}}_n^{(k)} = \tilde{\mathbf{X}}_{n,k}(t - t^{(k)})$.

Figure 4: Illustration of the time discretization of a particle's trajectory, and of the transport of the Stokeslet contributions by the undisturbed flow.

The functions d_1 and d_2 are singular both in space, at $r = \|\mathbf{x}\| = 0$, and in time, at $t = 0$. Following the exact same steps as in Section 3.3, we can derive an approximation of the Laplacian of the ε -weighted velocity disturbance, which reads as

$$\nabla^2 \mathbf{u}'_{n,\varepsilon}(\mathbf{x}, t) = \sum_{k=1}^K \mathbf{F}_n(t^{(k)}) \cdot \left[\mathcal{L}_{\mathcal{K}} \left(\mathbf{x} - \tilde{\mathbf{X}}_{n,k}(t - t^{(k)}), t - \tau \right) \right]_{\tau=t^{(k+1)}}^{\tau=t^{(k)}}, \quad (77)$$

where

$$\mathcal{L}_{\mathcal{K}} = \mathcal{K} \otimes \mathcal{L}, \quad (78)$$

and

$$\mathcal{L}(\mathbf{x}, t) = \int_0^t \boldsymbol{\ell}(\mathbf{x}, s) ds = \frac{1}{\mu} (\mathcal{I}\mathcal{D}_1(\|\mathbf{x}\|, t) + (\mathbf{x} \otimes \mathbf{x}) \mathcal{D}_2(\|\mathbf{x}\|, t)). \quad (79)$$

In the previous expression,

$$\mathcal{D}_1(r, t) = \int_0^t d_1(r, s) ds = \frac{1}{4\pi r^3} \left[1 + \frac{r(r^2 + 2\nu t)}{2\nu t \sqrt{\pi\nu t}} \exp\left(-\frac{r^2}{4\nu t}\right) - \operatorname{erf}\left(\frac{r}{\sqrt{4\nu t}}\right) \right], \quad (80)$$

$$\mathcal{D}_2(r, t) = \int_0^t d_2(r, s) ds = \frac{-3}{4\pi r^5} \left[1 + \frac{r(r^2 + 6\nu t)}{6\nu t \sqrt{\pi\nu t}} \exp\left(-\frac{r^2}{4\nu t}\right) - \operatorname{erf}\left(\frac{r}{\sqrt{4\nu t}}\right) \right]. \quad (81)$$

Alternatively, an approximation of $\nabla^2 \mathbf{u}'_{n,\varepsilon}$ could also be obtained by directly applying a discrete Laplacian operator to the vector field $\mathbf{u}'_{n,\varepsilon}$ given by Eq. (72).

4. Special cases

In this section are discussed special cases of isolated particles for which the model proposed in Section 3.3 recovers well-known analytical solutions found in the literature.

4.1. Fixed source in quiescent flow

Let us consider the case in which:

- The Reynolds number associated with the evolution of the n^{th} particle and its transfer of momentum is very small, i.e. the particle's effect on the flow can be considered as that of a fixed momentum source in quiescent fluid;
- The particle feeds a constant force $-\mathbf{F}_n$ back to the fluid.

In such a case, the linearized equations governing the particle-induced flow disturbance, in the frame of reference attached to the particle, read as

$$\nabla \cdot \mathbf{v}'_{n,\varepsilon} = 0, \quad (82)$$

$$\rho \frac{\partial \mathbf{v}'_{n,\varepsilon}}{\partial t} = -\nabla p'_{n,\varepsilon} + \mu \nabla^2 \mathbf{v}'_{n,\varepsilon} - \mathcal{K}(\|\mathbf{y}\|) \mathbf{F}_n. \quad (83)$$

The particle-induced, ε -weighted velocity disturbance is thus given by

$$\mathbf{v}'_{n,\varepsilon}(\mathbf{y}, t) = -\mathbf{F}_n \cdot \mathcal{S}_{\mathcal{K}}(\mathbf{y}, t), \quad (84)$$

which is simply the expression of the persistent, transient regularized Stokeslet centered at the location of the n^{th} particle. As t tends to infinity, we recover the expression of the steady regularized Stokeslet, as used for instance in [6, 31].

4.2. Fixed source in steady uniform flow

Let us now consider the case in which:

- The particle's effect on the flow can be considered as that of a fixed momentum source subject to uniform steady flow;

- The particle feeds a constant force $-\mathbf{F}_n$ back to the fluid, which is parallel to the undisturbed flow.

This corresponds, for instance, to the case of an isolated particle falling at terminal velocity in quiescent fluid. In such a case, the flow reaches a steady state for which the linearized equations governing the particle-induced disturbance, in the frame of reference attached to the particle, read as

$$\nabla \cdot \mathbf{v}'_{n,\varepsilon} = 0, \quad (85)$$

$$\rho \tilde{\mathbf{v}}_{n,\varepsilon} \cdot \nabla \mathbf{v}'_{n,\varepsilon} = -\nabla p'_{n,\varepsilon} + \mu \nabla^2 \mathbf{v}'_{n,\varepsilon} - \mathcal{K}(\|\mathbf{y}\|) \mathbf{F}_n. \quad (86)$$

The particle-induced ε -weighted velocity disturbance is thus given by

$$\mathbf{v}'_{n,\varepsilon}(\mathbf{y}, t) = -\mathbf{F}_n \cdot \mathcal{O}_{\mathcal{K}}^{\infty}(\mathbf{y}, \tilde{\mathbf{v}}_{n,\varepsilon}), \quad (87)$$

where $\mathcal{O}_{\mathcal{K}}^{\infty}$ is the regularized Oseenlet operator obtained from the spatial convolution of \mathcal{K} with the singular Oseenlet operator, \mathcal{O}^{∞} , as done in [6, 31]. Fundamentally, the Oseenlet operator can be obtained by time convolution of the transient Stokeslet advected at constant velocity in the direction of the uniform flow [44]. Therefore, in the limit of infinitesimal steps $t^{(k+1)} - t^{(k)}$, the model provided in Eq. (71) converges towards the steady regularized Oseenlet as given in Eq. (87).

5. Numerics

In this section, we discuss the implementation of the model proposed in Eq. (72) and study its convergence.

5.1. Determining the amount of previous instances needing to be stored

Storing all previous forcing instances considered in the sum of Eq. (72) evidently generates untractable computational costs when simulating particle-laden flows containing a significant amount of particles. Owing to the asymptotic behavior of the tensorial operator $\mathcal{S}_{\mathcal{K}}$ in time, however, it is clear that the most “recent” forcing instances are those mainly contributing to the particle-induced velocity disturbance, while the contributions of the “old” forcing instances become less and less significant as time increases.

For any monotonically decreasing radial kernel \mathcal{K} , the operator $\mathcal{S}_{\mathcal{K}}$ will typically generate maximum velocity contributions at $\mathbf{x} = \mathbf{0}$, where

$$\mathcal{S}_{\mathcal{K}}(\mathbf{0}, t) = \int_{\mathbb{R}^3} \mathcal{K}(\|\mathbf{y}\|) \mathcal{S}(\mathbf{y}, t) d\mathbf{y} = \mathcal{I} \left[\frac{4\pi}{\mu} \int_0^{\infty} \mathcal{K}(r) \left(r^2 \mathcal{H}_1(r, t) + \frac{r^4}{3} \mathcal{H}_2(r, t) \right) dr \right]. \quad (88)$$

The scalar integral in Eq. (88),

$$\mathcal{S}_{\mathcal{K}_0}(t) = \frac{4\pi}{\mu} \int_0^{\infty} \mathcal{K}(r) \left(r^2 \mathcal{H}_1(r, t) + \frac{r^4}{3} \mathcal{H}_2(r, t) \right) dr, \quad (89)$$

can generally be derived into a closed-form expression (see examples in Appendix A), and the ratio

$$\lambda_{\mathcal{K}}(m) = \frac{\mathcal{S}_{\mathcal{K}_0}(m\Delta t) - \mathcal{S}_{\mathcal{K}_0}((m-1)\Delta t)}{\mathcal{S}_{\mathcal{K}_0}(\Delta t)} \quad (90)$$

then approximates the importance of the m^{th} previous time instance relative to the most recent time instance in the discrete temporal convolution sum of Eq. (72). It can be shown that as m goes to infinity, the ratio $\lambda_{\mathcal{K}}(m)$ tends to zero as

$$\lambda_{\mathcal{K}}(m) \underset{m \rightarrow \infty}{\propto} m^{-3/2}. \quad (91)$$

For instance if \mathcal{K} is chosen as the gaussian filter \mathcal{G} of standard deviation σ , as defined in Eq. (A.6), then

$$\lambda_{\mathcal{G}}(m) = \frac{(2(m-1)\Delta t/\tau_{\nu} + \beta^2)^{-1/2} - (2m\Delta t/\tau_{\nu} + \beta^2)^{-1/2}}{\beta^{-1} - (2\Delta t/\tau_{\nu} + \beta^2)^{-1/2}}, \quad (92)$$

where τ_{ν} is the viscous time-scale associated with the filtering kernel defined as

$$\tau_{\nu} = \ell^2/\nu, \quad (93)$$

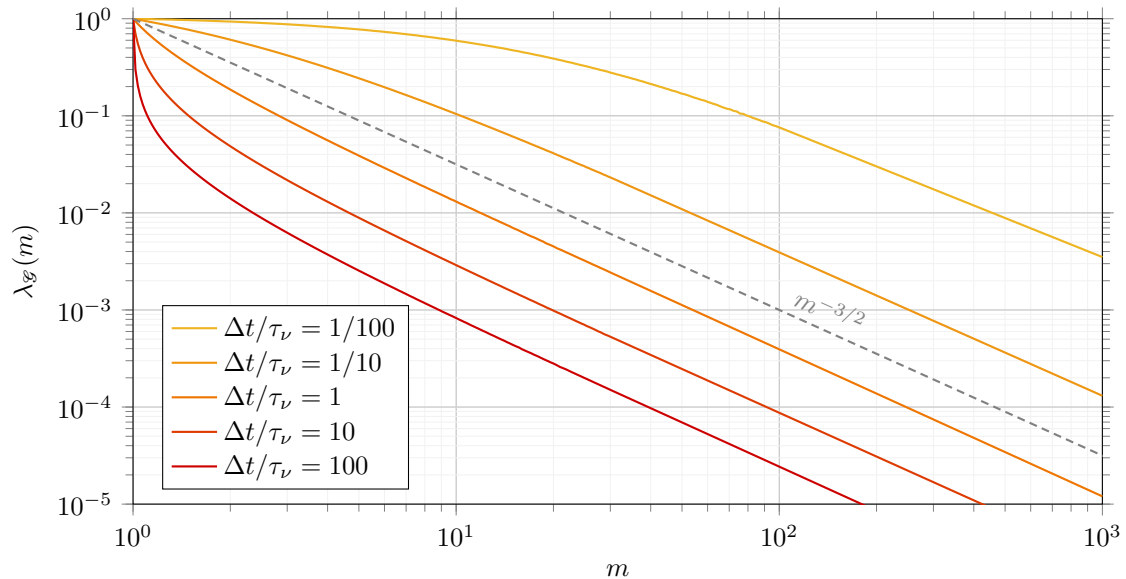


Figure 5: Importance of the m^{th} previous time instance relative to the most recent time instance, in the discrete temporal convolution sum of Eq. (72).

$\beta = \sigma/\ell$, and ℓ is the filter length-scale defined by Eq. (11). The ratio λ_g is plotted for different values of $\Delta t/\tau_\nu$ in Figure 5. From this figure, it is clear that the smaller $\Delta t/\tau_\nu$ is, the more previous time instances must be stored to accurately estimate the self-induced velocity disturbance according to Eq. (72). When $\Delta t = \tau_\nu$, the 20th previous forcing instance in Eq. (72) accounts for approximately less than 1% of the most recent forcing instance. When $\Delta t = 100\tau_\nu$, the 3rd previous forcing instance in Eq. (72) already accounts for less than 1% of the most recent forcing instance.

5.2. Computing the regularized transient Stokeslet/potential dipole tensorial operators

Deriving analytical expressions for the regularized transient Stokeslet and potential dipole tensorial operators, $\mathcal{S}_\mathcal{K}$ and $\mathcal{L}_\mathcal{K}$, is tedious or often even simply impossible. Their discrete computation, on the other hand, presents several advantages:

- Its implementation is relatively straightforward;
- It enables an arbitrary choice of filtering kernel \mathcal{K} ;
- It naturally adapts to the finite spatial and temporal resolutions of the Eulerian variable fields (and therefore of the particle-induced velocity disturbance generated by the numerical solution of the volume-filtered governing equations), if the same spatial resolution is used for the discrete convolution of the singular tensorial operators with the filtering kernel \mathcal{K} , and the same temporal resolution is used for their sampling over time;
- The discrete maps of the regularized tensorial operators can be computed once and for all in a pre-simulation step and stored in memory, resulting in a negligible cost overall;
- Using the symmetries of the filtering kernel and singular tensorial operators, the computational memory footprint of these solutions can be minimised.

We thus choose to discretely map, both in space and time, the regularized transient Stokeslet and potential dipole tensorial operators, $\mathcal{S}_\mathcal{K}$ and $\mathcal{L}_\mathcal{K}$. To that end, the singular tensorial operators, \mathcal{S} and \mathcal{L} , and the filtering kernel, \mathcal{K} , are spatially sampled on a grid of resolution $\Delta\hat{x}$ before being spatially convoluted. The resulting discrete maps of the regularized transient Stokeslet and potential dipole tensorial operators are generated at discrete times that are either sampled uniformly or logarithmically in time. If $\Delta\hat{x}$ is chosen smaller than the Eulerian grid resolution Δx , the regularized operators $\mathcal{S}_\mathcal{K}$ and $\mathcal{L}_\mathcal{K}$ are subjected to an additional spatial convolution with the top-hat kernel \mathcal{H} of radius $\sqrt[3]{3/4\pi}\Delta x$, so as to match the regularization imposed by our second-order finite-volume discretization. As mentioned in Section 3, the singular tensorial operators \mathcal{S} and \mathcal{L} are regular in time, but singular in space at $\mathbf{x} = \mathbf{0}$. With the aim to sample these two operators with (close to) second-order spatial accuracy, we employ the following strategy to calculate their discrete values at the sampling grid-points \mathbf{x}_i :

- If $\|\mathbf{x}_i\| < \Delta\hat{x}/2$,

$$\mathcal{S}_i^x(t) = \mathcal{S}_{\hat{\mathcal{H}}}(\mathbf{0}, t), \quad (94)$$

where $\hat{\mathcal{H}}$ is the top-hat filter compact on the ball of radius $\sqrt[3]{3/4\pi}\Delta\hat{x}$. The quantity $\mathcal{S}_{\hat{\mathcal{H}}}(\mathbf{0}, t)$ is derived in [Appendix A.1](#).

- Otherwise,

$$\mathcal{S}_i^x(t) = \mathcal{S}(\mathbf{x}_i, t). \quad (95)$$

A similar strategy is employed to spatially sample \mathcal{L} . The filtering kernel \mathcal{K} is spatially sampled in a similar manner as for the computation of ε or \mathbf{f} on the Eulerian grid. This discrete sampling and convolution process is illustrated in [Figure 6](#). Owing to the radially of the filtering kernel \mathcal{K} and the symmetries of \mathcal{S} and \mathcal{L} , it is sufficient to map one diagonal and one off-diagonal component of each tensor $\mathcal{S}_{\mathcal{K}}$ and $\mathcal{L}_{\mathcal{K}}$ in the top-right quadrant of the two-dimensional real space. Examples of the resulting two-dimensional maps are given in [Figure 7](#). Although the discrete convolutions of \mathcal{S} and \mathcal{L} with \mathcal{K} can be computed “naturally”, i.e. by calculating the convolution integrals with some numerical quadrature rule, the use of discrete Fourier transforms (DFT) can hugely speed up the process of generating the maps³.

In practice, after having generated the discrete maps, the following cases arise when interpolation $\mathcal{S}_{\mathcal{K}}(\mathbf{x}, t)$ or $\mathcal{L}_{\mathcal{K}}(\mathbf{x}, t)$ from them:

- If \mathbf{x} and t are located within the spatial and temporal scopes of the maps, then we use quadri-linear interpolation from the maps;
- If \mathbf{x} is outside the spatial scope of the maps, then we use the approximations $\mathcal{S}_{\mathcal{K}}(\mathbf{x}, t) \simeq \mathcal{S}(\mathbf{x}, t)$ and $\mathcal{L}_{\mathcal{K}}(\mathbf{x}, t) \simeq \mathcal{L}(\mathbf{x}, t)$, since far away from the singularity, the regularized tensorial operators converge towards their singular equivalents (see, e.g., [Figure 8](#));
- If t is outside the temporal scope of the maps and \mathbf{x} is within the spatial scope of the maps, we use the steady regularized tensorial operator (see, e.g., [Eq. \(97\)](#) for an expression of the steady tensorial operator regularized by the Wendland kernel).

³The convolution theorem specifies that the convolution of two functions is obtained from the inverse Fourier transform of the product of their respective Fourier transforms; $\phi \otimes \psi = \mathcal{F}^{-1}(\mathcal{F}(\phi) \cdot \mathcal{F}(\psi))$.

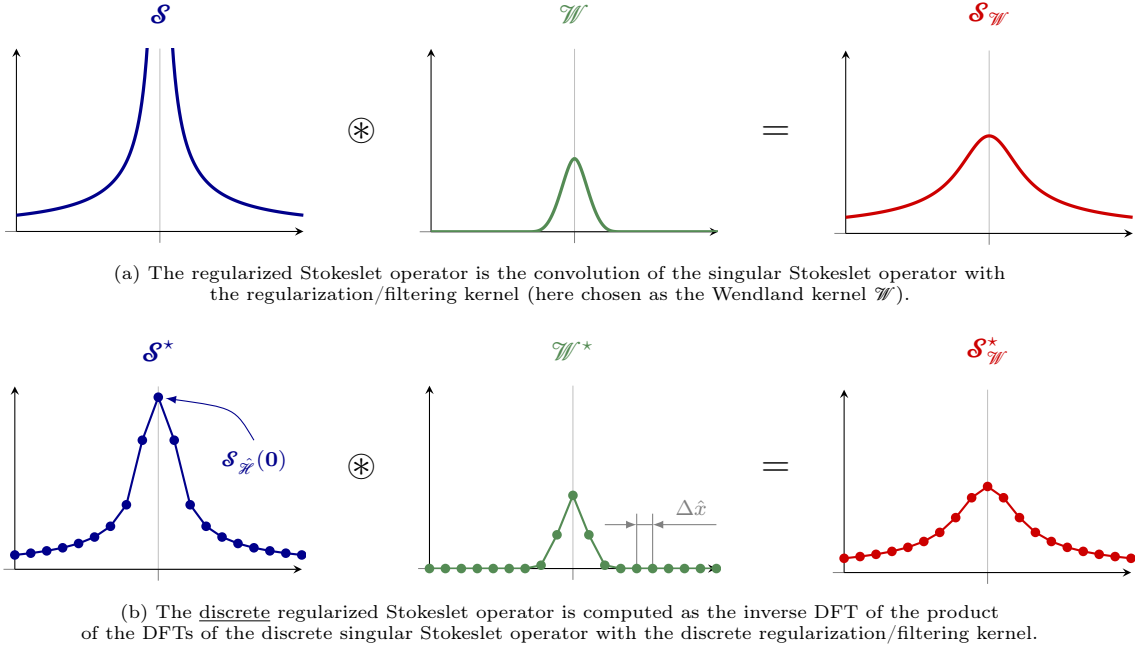


Figure 6: Schematic of the discrete convolution of the singular Stokeslet operator with the regularization kernel, highlighting the discrete sampling of the functions.

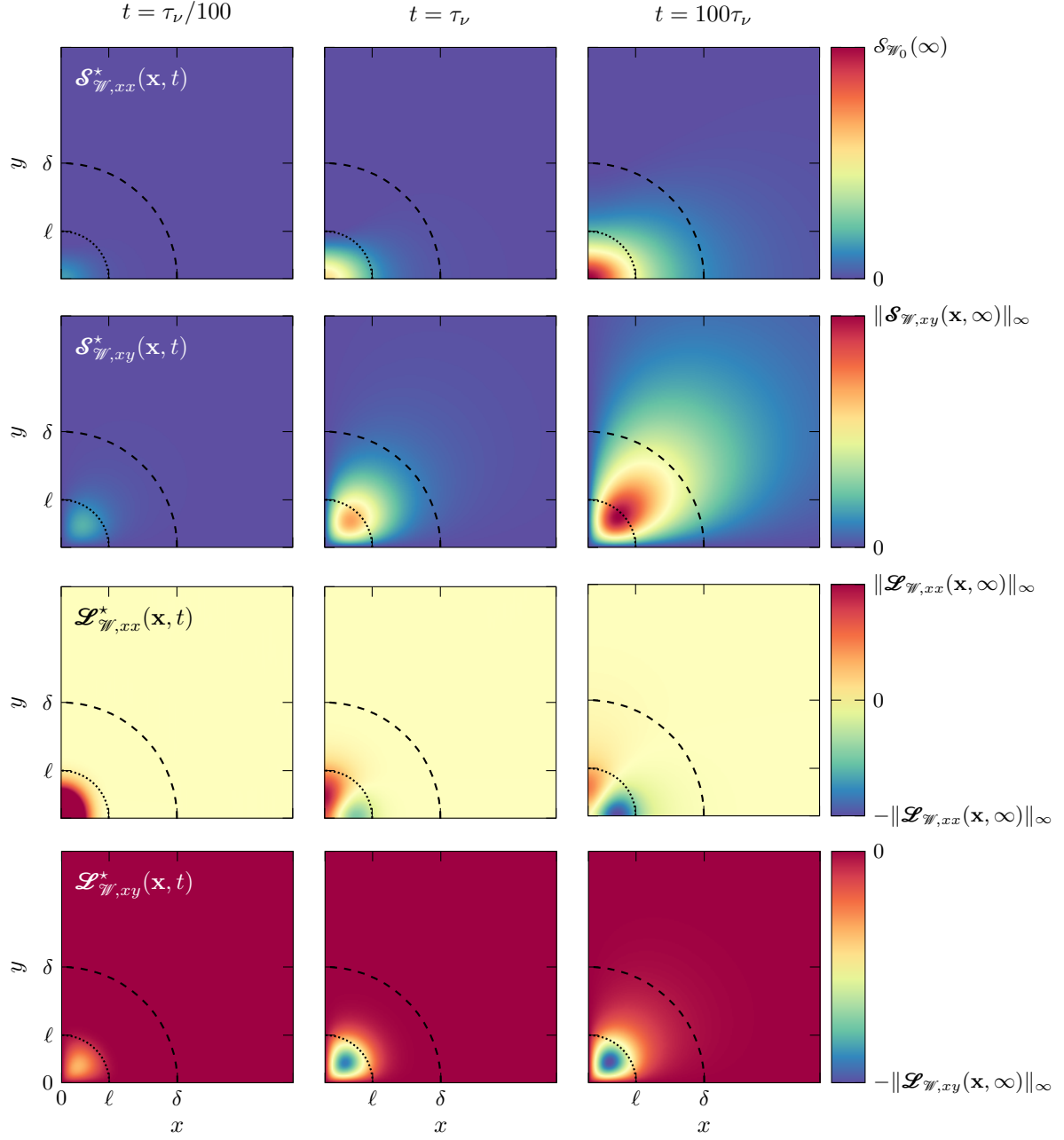


Figure 7: Example of discrete maps for the regularized transient Stokeslet and potential dipole tensors at three different times $t \in \{\tau_\nu/100, \tau_\nu, 100\tau_\nu\}$, and with \mathcal{K} chosen as the Wendland polynomial kernel \mathcal{W} , defined in Eq.(A.11), compactly supported on the ball of radius δ . The length-scale ℓ is defined by Eq. (11). The time-scale τ_ν is defined by Eq. (93).

Regularization of the steady Stokeslet operator

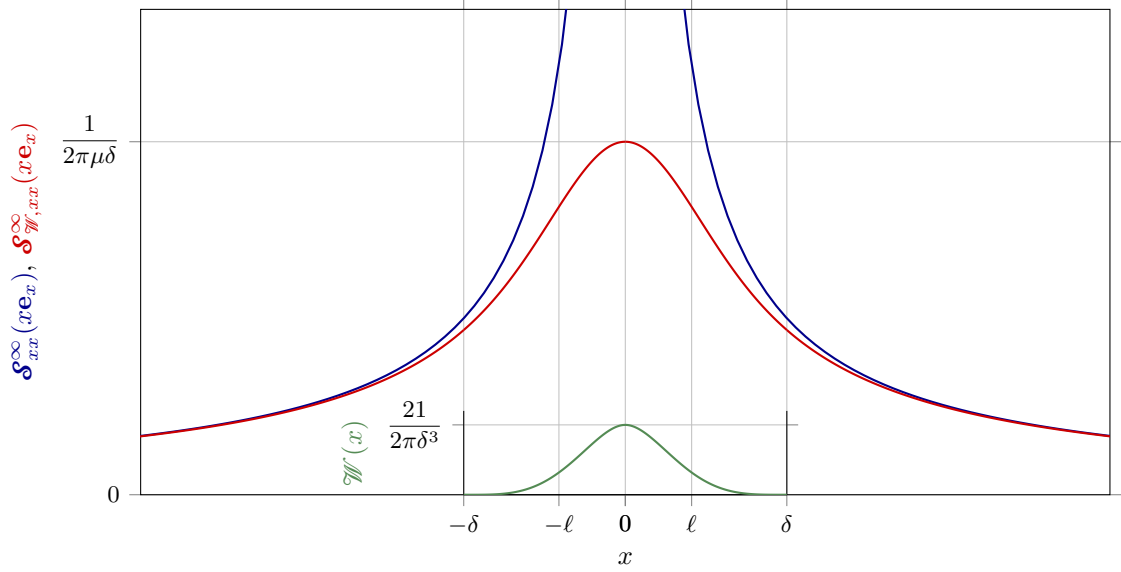


Figure 8: Diagonal coefficient of the singular and regularized Stokeslet operators, along the x -axis. The regularization kernel is the Wendland kernel, \mathcal{W} , defined in Eq. (A.11). The length-scale ℓ is defined by Eq. (11).

5.3. Spatial convergence

In this section, our aim is to assess the spatial convergence of the proposed model and, more generally, its performance at finite spatial resolution. To that end, we consider the spatial convolution of the singular, steady Stokeslet operator,

$$\mathcal{S}^\infty(\mathbf{x}) = \frac{1}{8\pi\mu\|\mathbf{x}\|} \left(\mathcal{I} + \frac{\mathbf{x} \otimes \mathbf{x}}{\|\mathbf{x}\|^2} \right), \quad (96)$$

with the Wendland kernel defined in Eq. (A.11). The corresponding regularized operator can be derived analytically [31, 45], and reads as

$$\mathcal{S}_{\mathcal{W}}^\infty(\mathbf{x}) = [\mathcal{S}^\infty \otimes \mathcal{W}](\mathbf{x}) = \frac{1}{8\pi\mu} \left(\mathcal{I} \mathcal{H}_{1,\mathcal{W}}^\infty(\|\mathbf{x}\|) + (\mathbf{x} \otimes \mathbf{x}) \mathcal{H}_{2,\mathcal{W}}^\infty(\|\mathbf{x}\|) \right), \quad (97)$$

where

$$\mathcal{H}_{1,\mathcal{W}}^\infty(r) = \begin{cases} \frac{-81r^7 + 400r^6\delta - 735r^5\delta^2 + 540r^4\delta^3 - 168r^2\delta^5 + 60\delta^7}{15\delta^8}, & \text{if } r < \delta \\ \frac{1}{r} + \frac{\delta^2}{15r^3}, & \text{if } r \geq \delta \end{cases}, \quad (98)$$

$$\mathcal{H}_{2,\mathcal{W}}^\infty(r) = \begin{cases} \frac{21r^5 - 100r^4\delta + 175r^3\delta^2 - 120r^2\delta^3 + 28\delta^5}{5\delta^8}, & \text{if } r < \delta \\ \frac{1}{r^3} - \frac{\delta^2}{5r^5}, & \text{if } r \geq \delta \end{cases}. \quad (99)$$

The first diagonal component of these singular and regularized operators, along the x -axis, is shown in Figure 8. Note that we recover the classical result that, at distances much larger than the length-scale associated with the convolution kernel, the regularized Stokeslet operator converges towards the singular Stokeslet,

$$\lim_{\|\mathbf{x}\| \rightarrow \infty} (\mathcal{S}_{\mathcal{W}}^\infty(\mathbf{x}) - \mathcal{S}^\infty(\mathbf{x})) = \underline{\underline{0}}. \quad (100)$$

As described in Section 5.2, the proposed discrete execution of the spatial convolution between \mathcal{W} and \mathcal{S}^∞ requires their sampling on a grid of uniform spacing $\Delta\hat{x}$. The discrete samples of \mathcal{W} are computed with the adaptive quadrature rule presented in [19]. The discrete samples of \mathcal{S}^∞ are computed as described in Section 5.2, in order to treat the singularity at $\mathbf{x} = \mathbf{0}$. This means that the singular steady Stokeslet

is sampled at \mathbf{x}_i , the location of the i^{th} sampling point, as follows:

$$\mathcal{S}_i^{*,\infty} = \begin{cases} \mathcal{I}(4\pi\mu\alpha\Delta\hat{x})^{-1} & \text{if } \|\mathbf{x}_i\| < \Delta\hat{x}/2 \\ \mathcal{S}^\infty(\mathbf{x}_i) & \text{otherwise} \end{cases}, \quad (101)$$

with $\alpha = \sqrt[3]{3/(4\pi)}$. Once \mathcal{W} and \mathcal{S}^∞ have been discretely sampled into \mathcal{W}^* and $\mathcal{S}^{*,\infty}$, the corresponding (discrete) regularized operator is obtained by computing the inverse DFT of the product of their DFTs.

In order to determine the order of spatial convergence of the proposed model, the relative error between the discrete regularized operator and its analytical counterpart is computed at $\mathbf{x}_0 = \mathbf{0}$ (where both operators are diagonal, by construction). We consider two errors, defined as

$$E_{\Delta\hat{x}} = \frac{|\text{tr}(\mathcal{S}_{\mathcal{W},0}^{*,\infty}) - \text{tr}(\mathcal{S}_{\mathcal{W}}^\infty(\mathbf{0}))|}{|\text{tr}(\mathcal{S}_{\mathcal{W}}^\infty(\mathbf{0}))|}, \quad (102)$$

$$\bar{E}_{\Delta\hat{x}} = \frac{|\text{tr}(\mathcal{S}_{\mathcal{W},0}^{*,\infty}) - \text{tr}(\mathcal{S}_{\mathcal{W},\tilde{\mathcal{H}}}^\infty(\mathbf{0}))|}{|\text{tr}(\mathcal{S}_{\mathcal{W},\tilde{\mathcal{H}}}^\infty(\mathbf{0}))|}. \quad (103)$$

The former error, $E_{\Delta\hat{x}}$, is the relative difference between the discrete regularized Stokeslet in the cell centered at $\mathbf{x}_0 = \mathbf{0}$ and the exact corresponding regularized Stokeslet evaluated at \mathbf{x}_0 . The latter error, $\bar{E}_{\Delta\hat{x}}$, is the relative difference between the discrete regularized Stokeslet in the cell centered at \mathbf{x}_0 and an approximation of the average of the exact regularized Stokeslet in the cell centered at \mathbf{x}_0 (this average is estimated by convolution of the exact regularized Stokeslet with the top-hat kernel of radius $\sqrt[3]{3/4\pi}\Delta\hat{x}$). At high resolution ($\delta/\Delta\hat{x} \gg 1$), we should expect both errors to exhibit a similar behavior, since the difference between the exact regularized Stokeslet evaluated at \mathbf{x}_0 and its average in the cell centered at \mathbf{x}_0 decreases as resolution increases. At low resolution ($\delta/\Delta\hat{x} \ll 1$) we should expect both errors to behave differently: The error $\bar{E}_{\Delta\hat{x}}$ should reach the asymptotic value of 1, since

$$\lim_{\delta/\Delta\hat{x} \rightarrow 0} \mathcal{S}_{\mathcal{W},0}^{*,\infty} = \underline{\mathbf{0}}, \quad (104)$$

while $\mathcal{S}_{\mathcal{W}}^\infty(\mathbf{0}) = \mathcal{I}(2\pi\delta\mu)^{-1} \neq \underline{\mathbf{0}}$. The error $\bar{E}_{\Delta\hat{x}}$, on the other hand, should converge towards zero as $\delta/\Delta\hat{x}$ decreases. These behaviors are indeed verified by the results plotted in Figure 9a.

5.4. Temporal convergence

In this section, our aim is to assess the temporal convergence of the proposed model. To that end, we consider the spatial convolution of the singular, steady Oseenlet operator [43],

$$\mathcal{O}^\infty(\mathbf{x}) = \frac{1}{8\pi\mu} (\mathcal{I}\mathcal{Q}_1^\infty(\mathbf{x}) - \nabla\mathcal{Q}_2^\infty(\mathbf{x})), \quad (105)$$

where

$$\mathcal{Q}_1^\infty(\mathbf{x}) = \frac{2 \exp(-\xi(\mathbf{x}))}{\|\mathbf{x}\|}, \quad (106)$$

$$\mathcal{Q}_2^\infty(\mathbf{x}) = \frac{1 - \exp(-\xi(\mathbf{x}))}{\xi(\mathbf{x})} \left(\frac{\mathbf{x}}{\|\mathbf{x}\|} - \frac{\tilde{\mathbf{u}}}{\|\tilde{\mathbf{u}}\|} \right), \quad (107)$$

$$\xi(\mathbf{x}) = \frac{\|\tilde{\mathbf{u}}\|\|\mathbf{x}\| - \tilde{\mathbf{u}} \cdot \mathbf{x}}{2\nu}, \quad (108)$$

with the Wendland kernel defined in Eq. (A.11). Assuming that $\tilde{\mathbf{u}}$ is aligned with \mathbf{e}_x , the first diagonal component of the regularized Oseenlet operator, at $\mathbf{x} = \mathbf{0}$, reads as [6, 31]

$$\mathcal{O}_{\mathcal{W},xx}^\infty(\mathbf{0}) = \frac{\Psi_{\mathcal{W}}(\text{Re}_\delta)}{2\pi\delta\mu}, \quad (109)$$

where

$$\text{Re}_\delta = \frac{\delta\|\tilde{\mathbf{u}}\|}{\nu}, \quad (110)$$

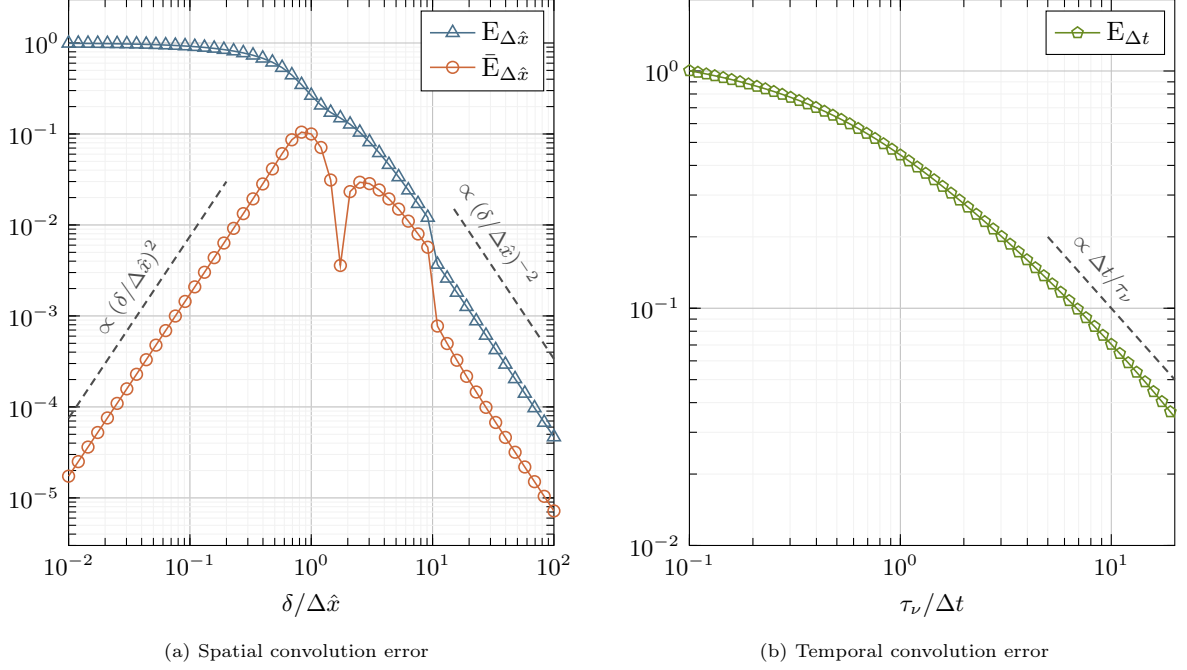


Figure 9: In both graphs, the Wendland kernel defined in Eq. (A.11) is used as regularization kernel: (a) Relative errors between the discrete and analytical regularized steady Stokeslet operators, computed at the origin. The error is shown as a function of the ratio between δ , the radius of the Wendland kernel’s support, and Δx , the spacing of the sampling grid for the discrete convolution; (b) Relative error between the discrete and analytical regularized Oseenlet operators, computed at the origin. The error is shown as a function of the ratio between the viscous time-scale of the kernel, τ_ν , and Δt , the timestep used to discretize the temporal convolution integral.

δ being the radius of the Wendland kernel’s support, and $\Psi_{\mathcal{W}}$ is the function given by

$$\Psi_{\mathcal{W}}(x) = 7 \left(x^{-1} - 6x^{-2} + 30x^{-3} - 120x^{-4} + 360x^{-5} - 720x^{-6} + 720x^{-7} (1 - \exp(-x)) \right). \quad (111)$$

For vanishing Reynolds numbers,

$$\lim_{\text{Re}_\delta \rightarrow 0} \Psi_{\mathcal{W}}(\text{Re}_\delta) = 1, \quad (112)$$

and one recovers the regularized steady Stokeslet solution derived in Appendix A.3,

$$\lim_{\text{Re}_\delta \rightarrow 0} \mathcal{O}_{\mathcal{W},xx}^\infty(\mathbf{0}) = \mathcal{S}_{\mathcal{W},xx}^\infty(\mathbf{0}) = \frac{1}{2\pi\delta\mu}. \quad (113)$$

The ratio $\Psi_{\mathcal{W}}$ of the steady Oseenlet and Stokeslet operators regularized by the Wendland kernel, at the location of the origin $\mathbf{x} = \mathbf{0}$, is plotted in Figure 10 as a function of the Reynolds number Re_δ . Note that the ratio $\Psi_{\mathcal{G}}$ corresponding to the regularization by the Gaussian kernel \mathcal{G} , defined in Eq (A.6), has been derived by Balachandar et al. [6], and that its piecewise approximation based on Taylor series expansions that mitigates round-off errors is provided in [31].

Importantly for the current temporal convergence analysis and as mentioned in Section 4.2, it is possible to recover the singular steady Oseenlet operator by calculating the limit, as $t \rightarrow \infty$, of the time convolution of the singular transient Stokeslet operator, \mathcal{J} , travelling with the velocity $\tilde{\mathbf{u}}$ [44], i.e.,

$$\mathcal{O}^\infty(\mathbf{x}) = \lim_{t \rightarrow \infty} \int_0^t \mathcal{J}(\mathbf{x} - (t - \tau)\tilde{\mathbf{u}}, t - \tau) d\tau. \quad (114)$$

The regularized Oseenlet operator then reads as

$$\mathcal{O}_{\mathcal{W}}^\infty(\mathbf{x}) = \lim_{t \rightarrow \infty} \int_{\mathbb{R}^3} \int_0^t \mathcal{W}(\|\mathbf{x} - \mathbf{r}\|) \mathcal{J}(\mathbf{x} - (t - \tau)\tilde{\mathbf{u}}, t - \tau) d\tau d\mathbf{r}. \quad (115)$$

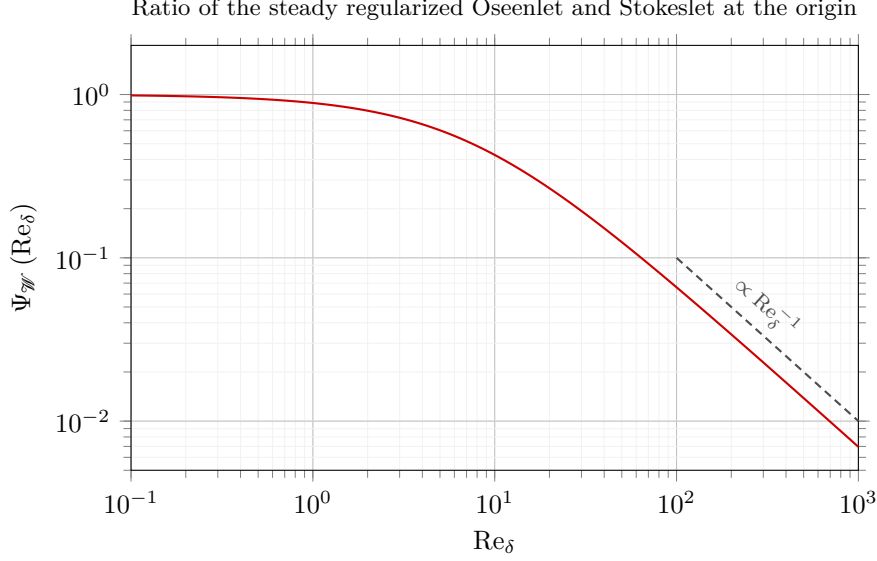


Figure 10: Ratio of the steady regularized Oseenlet and Stokeslet at the origin $\mathbf{x} = 0$ for the component aligned with the background flow velocity vector $\tilde{\mathbf{u}}$. At low Reynolds number, this ratio is close to 1, meaning that the steady regularized Oseenlet and Stokeslet operators are identical. At high Reynolds number, this ratio becomes inversely proportional to the Reynolds number [6], meaning that the magnitude of the Oseenlet vanishes compared to the Stokeslet.

Applying the same time discretization as in Section 3, this regularized operator can be approximated as

$$\mathcal{O}_{\mathcal{W}}^{\infty}(\mathbf{x}) \simeq \mathcal{O}_{\mathcal{W},\Delta t}^{\infty}(\mathbf{x}) = \sum_{k=1}^{\infty} [\mathcal{S}_{\mathcal{W}}(\mathbf{x} - \tilde{\mathbf{u}}(k-1)\Delta t, \tau)]_{\tau=(k-1)\Delta t}^{\tau=k\Delta t}, \quad (116)$$

where $\mathcal{S}_{\mathcal{W}}$ is the time-persistent transient Stokeslet operator regularized by the Wendland kernel. In the context of the volume-filtered modeling of particle-laden flow, this simply corresponds to the (somewhat conceptual) case of a fixed particle, subject to a uniform undisturbed flow $\tilde{\mathbf{u}}$, and feeding a constant force back to the fluid. In order to study the temporal convergence of the model, we further approximate the previous equation as

$$\mathcal{O}_{\mathcal{W},\Delta t}^{\infty}(\mathbf{x}) = \sum_{k=1}^K [\mathcal{S}_{\mathcal{W}}(\mathbf{x} - \tilde{\mathbf{u}}(k-1)\Delta t, \tau)]_{\tau=(k-1)\Delta t}^{\tau=k\Delta t}, \quad (117)$$

where K is chosen such that the regularized transient Stokeslet contributions for $k > K$ are negligible. In Eq. (117), $\mathcal{S}_{\mathcal{W}}$ is interpolated from discrete maps that are generated by the process described in Section 5.2. We choose K such that $K\Delta t \simeq 1000\tau_{\nu}$ and $\delta/\Delta x = 100$, so as to make sure that the error of the model is dominated by the time discretization, instead of the limited number of steps taken or the spatial resolution of the discrete maps. The width of the discrete maps chosen equal to 10δ . Outside this scope, the regularized transient Stokeslet operator, $\mathcal{S}_{\mathcal{W}}$, is approximated by its singular (analytical) counterpart, \mathcal{S} , since the difference between these two operators vanishes far away from the singularity. Moreover, we choose $\text{Re}_{\delta} = 10$ in order for the regularized Oseenlet operator, $\mathcal{O}_{\mathcal{W}}^{\infty}$, to differ greatly from the regularized Stokeslet operator, $\mathcal{S}_{\mathcal{W}}^{\infty}$. This latter choice of a finite Reynolds number is necessary because, in the limit of a vanishing Reynolds number, Eq. (116) provides an approximation of $\mathcal{O}_{\mathcal{W}}^{\infty}$ that is independent of the value of Δt .

The error of the model due to time discretization is calculated as the relative error between the first diagonal component of the discrete regularized Oseenlet operator, as given by Eq. (117), and its analytical counterpart, given by Eq. (109),

$$E_{\Delta t} = \frac{|\mathcal{O}_{\mathcal{W},\Delta t,xx}^{\infty}(\mathbf{0}) - \mathcal{O}_{\mathcal{W},xx}^{\infty}(\mathbf{0})|}{|\mathcal{O}_{\mathcal{W},xx}^{\infty}(\mathbf{0})|}. \quad (118)$$

As expected from our use of a left-hand integration rule to estimate the convolution integral in Eq. (68), the results plotted in Figure 9b confirm the first-order accuracy of our discrete time convolution.

6. Results

In this section, the model introduced in Section 3 is used to approximate the particle’s self-induced velocity disturbance – and therefore recover the undisturbed velocity associated with that particle – for cases of isolated particles with prescribed motion or freely evolving within the fluid. For ease of implementation, we neglect the unclosed terms \mathcal{Z}_{Re} and \mathcal{Z}_{μ} , as well as $\partial\varepsilon/\partial t$ in the volume-filtered governing equations. Thus, they simplify to

$$\nabla \cdot \bar{\mathbf{u}}_\varepsilon = 0, \quad (119)$$

$$\rho \left(\frac{\partial \bar{\mathbf{u}}_\varepsilon}{\partial t} + \nabla \cdot (\bar{\mathbf{u}}_\varepsilon \otimes \bar{\mathbf{u}}_\varepsilon) \right) = -\nabla \bar{p}_\varepsilon + \mu \nabla^2 \bar{\mathbf{u}}_\varepsilon + \mathbf{f}, \quad (120)$$

which correspond to the incompressible Navier-Stokes equations for the superficial velocity $\bar{\mathbf{u}}_\varepsilon$ and pressure \bar{p}_ε , subject to a momentum source \mathbf{f} . Owing to this choice, we can use any conventional incompressible flow solver to test our model, the effect that the particles have on the flow only appearing in the form of the momentum source \mathbf{f} .

In the following subsections, the second-order finite-volume framework of Denner et al. [46] is used to solve the set of governing equations (119) and (120). The Wendland kernel \mathcal{W} , defined in Eq. (A.11), is employed for the regularization of the momentum source and is therefore also considered for the production of the discrete regularized transient Stokeslet maps required by the proposed model. Unless specified otherwise, velocity is interpolated at the location of a particle using tri-linear interpolation, and no limit is set for the integer K in Eq. (72). This means that all previous forcing time instances are considered for approximating the particle’s self-induced velocity disturbance at a given time. This choice has been made to showcase the full potential of the model, although having no limit for K would naturally lead to untractable computational cost in the context of real large-scale particle-laden flows. In practice, a limit must be specified for K based on computational cost and/or accuracy considerations (see Sections 5.1 and 6.4).

6.1. Fixed particle in uniform flow

In a first instance, we consider the case of a fixed particle subject to uniform flow with the constant velocity $\tilde{\mathbf{u}}$. The particle Reynolds number is defined as

$$\text{Re}_n = \frac{d_n \|\tilde{\mathbf{u}}\|}{\nu}, \quad (121)$$

where d_n is the diameter of the particle. In each case, the fixed particle feeds back to the fluid a momentum contribution corresponding to the opposite of the steady drag force acting on the particle,

$$\mathbf{f} = -3\pi\mu d_n \tilde{\mathbf{u}} f(\text{Re}_n) \mathcal{W}(\|\mathbf{x}\|), \quad (122)$$

where $f(\text{Re}_n)$ is the Schiller and Naumann [10] empirical correction factor given as

$$f(\text{Re}_n) = 1 + 0.15 \text{Re}_n^{0.687}. \quad (123)$$

The radius of the kernel’s support is chosen equal to 2 particle diameters, i.e., $\delta = 2d_n$. This corresponds to a filter length-scale $\ell \simeq 0.8d_n$. For each simulation, the computational domain is chosen to be a cubic box with an edge-length equal to or greater than $L = 100d_n$. The center of this domain coincides with the center of the fixed particle, and a constant mesh-spacing Δx is applied over a distance of at least 3δ on each side of the particle. Outside of this region, the mesh-spacing is stretched so as to avoid unnecessary computational costs. The following parameter space is considered for choosing Δx and the fluid properties:

- $d_n/\Delta x \in \{\frac{1}{8}, \frac{1}{4}, \frac{1}{2}, 1, 2, 4\}$
- $\text{Re}_n \in \{\frac{1}{100}, \frac{1}{10}, 1, 10, 100\}$

Finally, in order to resolve the entire transient evolution of the particle’s self-induced flow disturbance, the solver timestep is initially chosen as

$$\Delta t = \frac{\tau_\star}{1000}, \quad (124)$$

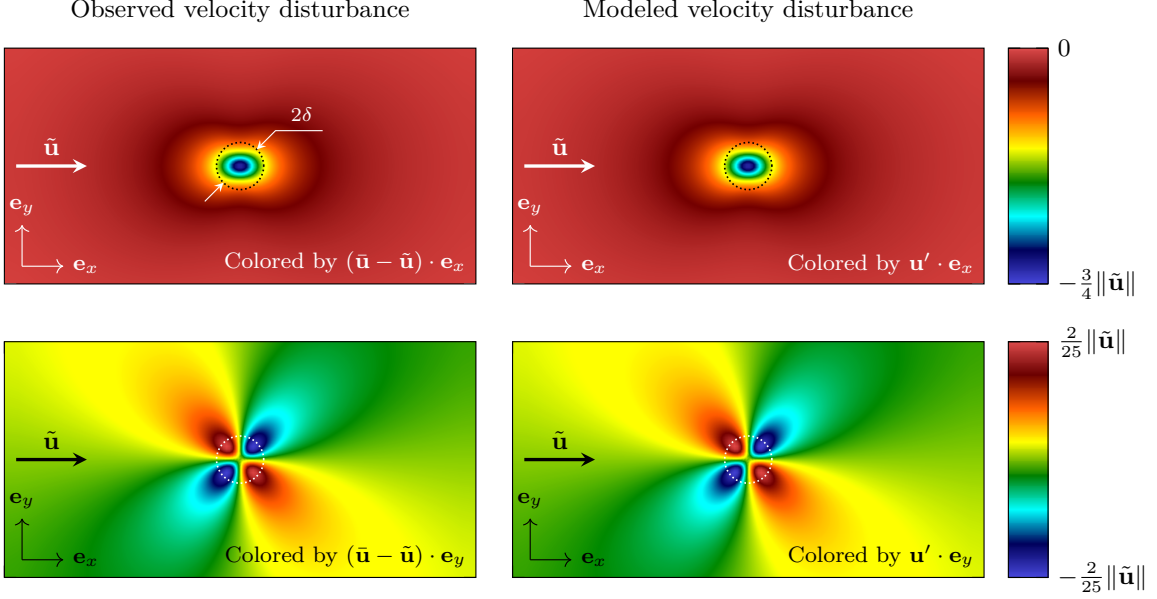


Figure 11: Snapshots of the simulation of a fixed particle subject to uniform flow, once steady state has been reached at $\text{Re}_n = 0.01$, with $d_n/\Delta x = 4$ and $\delta = 2d_n$. The left column shows the observed velocity disturbance obtained as the solution of the volume-filtered governing equations (119) and (120) from which is subtracted the undisturbed velocity $\tilde{\mathbf{u}}$. The right column shows its reconstruction obtained with the model proposed in Eq. (72).

where

$$\tau_\star = \frac{\ell_\star^2}{\nu} = \tau_\nu \left(\frac{\ell}{\ell_\star} \right)^2, \quad (125)$$

and

$$\ell_\star = \max(\ell, \Delta x \sqrt[3]{3/8\pi}). \quad (126)$$

The modified viscous time-scale τ_\star accounts for the fact that the computational grid acts as a top-hat filter of equivalent radius $\Delta x \sqrt[3]{3/8\pi}$, whose length-scale can become larger than ℓ at small $d_n/\Delta x$ ratio. At the end of each time iteration, Δt is increased by a factor 1.1 unless the CFL limit has been reached.

Figures 11 and 12 show snapshots of the simulations once a steady state has been reached at $\text{Re}_n = 0.01$ and $\text{Re}_n = 100$, with $d_n/\Delta x = 4$. The left columns show the observed velocity disturbance induced by the particle, obtained by subtracting the undisturbed velocity $\tilde{\mathbf{u}}$ from the filtered velocity $\bar{\mathbf{u}}$ solution to the volume-filtered governing equations (119) and (120). The right columns show its reconstruction obtained with the proposed model of Eq. (72). As such, the left columns display results of the flow solver, whereas the right columns display discrete fields reconstructed from the sum of analytical transient regularized Stokelets contributions. Qualitative differences between the observed and reconstructed flow disturbances are hardly perceivable, suggesting that the proposed model estimates the particle's self-induced velocity disturbance with good (qualitative) accuracy.

A quantitative analysis of the proposed model is shown in Figures 13, 14, and 15. Figure 13 displays the normalized velocity disturbance interpolated to the center of the particle at $\text{Re}_n = 0.01$ and for $d_n/\Delta x \in \{\frac{1}{8}, \frac{1}{4}, \frac{1}{2}, 1, 2, 4\}$. In the left plot, the disturbance is calculated as the difference between the x -components of the undisturbed velocity, $\tilde{\mathbf{u}}$, and the filtered velocity, $\bar{\mathbf{u}}$, interpolated to the particle center. It is then normalized by the norm of the undisturbed velocity $\tilde{\mathbf{u}}$. In the right plot, this value is corrected by further subtracting the velocity disturbance modeled by Eq. (72). The left and right plots therefore display the relative errors that would be made in the estimation of the fluid force acting on the particle when not using our model (left) and when using it (right). With infinite time and space resolution and in the limit of vanishing Reynolds number, our model should produce no error, which is illustrated by the limit-case ($\text{Re}_n = 0.01, d_n/\Delta x = 4$) for which the relative error is about 0.2% at most. Figure 14 displays the same normalized velocity disturbance interpolated to the center of the particle for $d_n/\Delta x = 4$ and at $\text{Re}_n \in \{\frac{1}{100}, \frac{1}{10}, 1, 10, 100\}$. Finally, Figure 15 summarizes this study by showing the

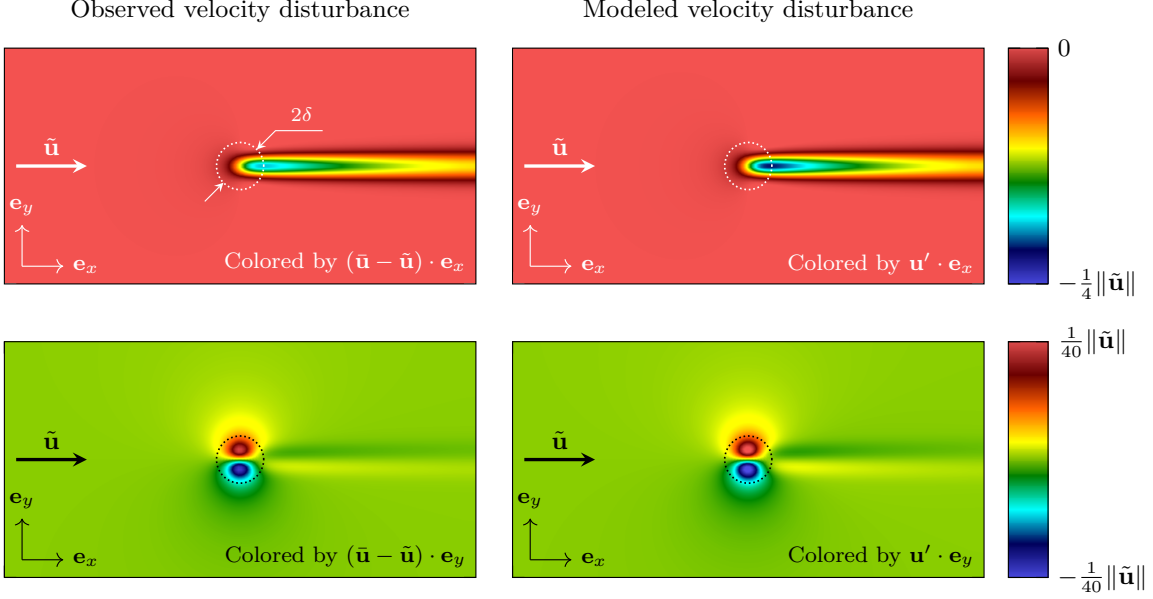


Figure 12: Snapshots of the simulation of a fixed particle subject to uniform flow, once steady state has been reached at $Re_n = 100$, with $d_n/\Delta x = 4$ and $\delta = 2d_n$. The left column shows the observed velocity disturbance obtained as the solution of the volume-filtered governing equations (119) and (120) from which is subtracted the undisturbed velocity $\tilde{\mathbf{u}}$. The right column shows its reconstruction obtained with the model proposed in Eq. (72).

maximum error made with/without correction across the tested parameter space. Without correction, i.e., by interpolating the filtered velocity at the particle location to estimate drag, a maximum relative error of almost 75% can be made. When using our proposed model to correct this interpolated filtered velocity, the maximum relative error that is made is reduced to about 10% at most.

Several interesting observations can be made from Figures 13, 14, and 15. First, it is clear that when no correction is applied, the magnitude of the particle’s self-induced velocity disturbance increases with the ratio $d_n/\Delta x$ and decreases with increasing Reynolds number. This is a well-known result of the VF-EL literature [6, 16, 26, 27, 31]. Second, it is apparent that at high mesh resolution, our model’s bottom performance is reached for Re_n around 10. As shown by the evolution of the coefficient $\Psi_{\mathcal{M}}$ as a function of the Reynolds number (see Eq. (111)), the magnitude of the particle’s self-induced velocity disturbance decreases proportional to the inverse of the Reynolds number. The case $Re_n \sim 10$ thus corresponds to the “worst-case” scenario in which the magnitude of the self-induced velocity disturbance is still relatively significant while non-linear effect are also important, therefore approaching the limits of our model built upon linearized governing equations.

6.2. Oscillating particle in uniform flow

We now consider the case of a particle subject to a prescribed oscillatory motion in a uniform flow with the constant fluid velocity $\tilde{\mathbf{u}}$. This case aims to test the performance of our model for predicting the particle’s self-induced velocity disturbance in a highly transient environment where the resultant of the fluid forces acting on the particle is not aligned with the undisturbed flow velocity.

The numerical setup and considered parameter space are identical to those of Section 6.1. The main difference lies in the particle having a prescribed motion instead of being fixed. This prescribed motion is given as

$$\mathbf{X}_n(t) = 5d_n \begin{bmatrix} \sin(4\omega t) \\ \sin(4\omega t) \cos(\omega t) \\ \sin(4\omega t) \sin(\omega t) \end{bmatrix}, \quad (127)$$

with

$$\omega = \frac{\pi \|\tilde{\mathbf{u}}\|}{25d_n}. \quad (128)$$

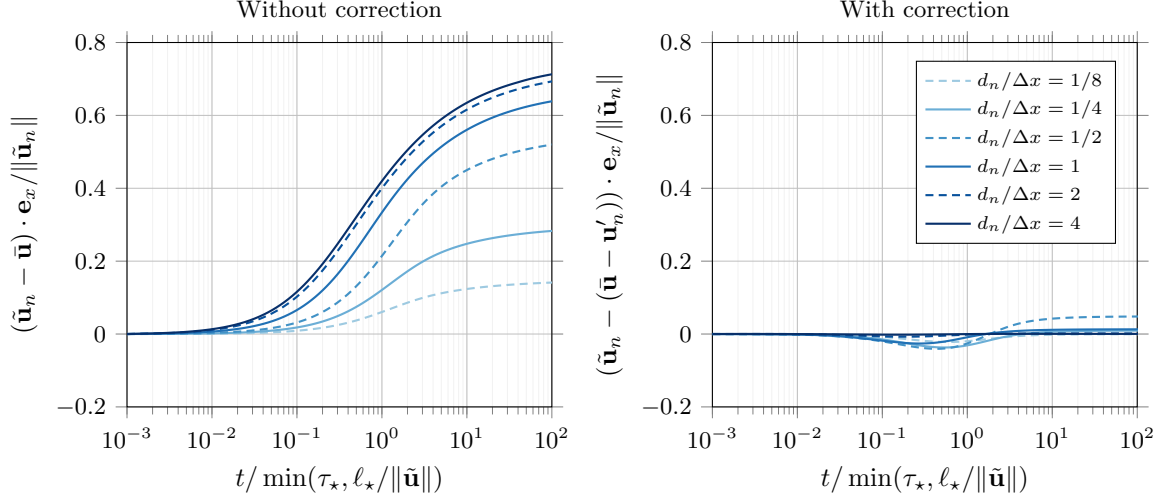


Figure 13: Relative error made in the estimation of the undisturbed velocity at the location of the fixed particle without (left) and with (right) the proposed modeled correction (using Eq. (72)). In this figure, the Reynolds number is fixed to $Re_n = 0.01$ while $d_n/\Delta x$ is varied in $\{\frac{1}{8}, \frac{1}{4}, \frac{1}{2}, 1, 2, 4\}$.

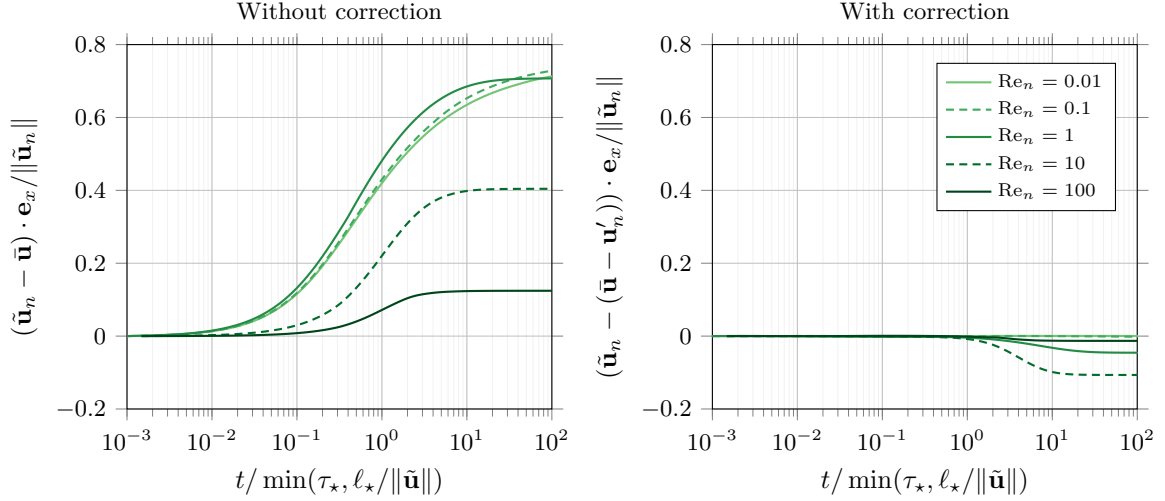


Figure 14: Relative error made in the estimation of the undisturbed velocity at the location of the fixed particle without (left) and with (right) the proposed modeled correction (using Eq. (72)). In this figure, the resolution is fixed to $d_n/\Delta x = 4$ while the Reynolds number is varied in $\{\frac{1}{100}, \frac{1}{10}, 1, 10, 100\}$.

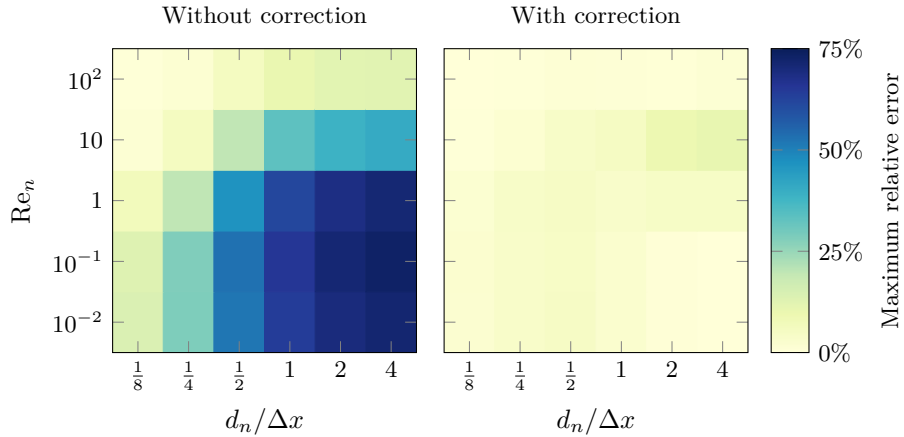


Figure 15: Maximum relative error made in the estimation of the undisturbed velocity at the location of the fixed particle without (left) and with (right) the proposed modeled correction (using Eq. (72)). The values are taken inside the time interval $[10^{-3}, 10^2] \times \min(\tau_*, \ell_*/\|\tilde{\mathbf{u}}\|)$.

This corresponds to a period of oscillation, $T = \pi/2\omega$, approximately varying between $0.02\tau_\nu$ and $200\tau_\nu$ across the chosen parameter space. The velocity of the particle is given as

$$\mathbf{U}_n(t) = 5d_n \begin{bmatrix} 4\omega \cos(4\omega t) \\ 4\omega \cos(4\omega t) \cos(\omega t) - \omega \sin(4\omega t) \sin(\omega t) \\ 4\omega \cos(4\omega t) \sin(\omega t) + \omega \sin(4\omega t) \cos(\omega t) \end{bmatrix}. \quad (129)$$

The particle feeds back to the fluid a momentum contribution corresponding to the opposite of the steady drag force acting on the particle,

$$\mathbf{f}(t) = -3\pi\mu d_n (\tilde{\mathbf{u}} - \mathbf{U}_n(t)) f(\text{Re}_n) \mathcal{W}(\|\mathbf{x} - \mathbf{X}_n(t)\|), \quad (130)$$

where $f(\text{Re}_n)$ is the Schiller and Naumann [10] empirical correction factor given in Eq. (123). The solver timestep is chosen as the minimum between

$$\Delta t = \frac{d_n}{10\|\tilde{\mathbf{u}}\|}, \quad (131)$$

and the timestep enforcing $\text{CFL} = 0.1$.

Figures 16 and 17 show snapshots of the simulations at $\text{Re}_n = 1$ and $\text{Re}_n = 10$, with $d_n/\Delta x = 4$. The left columns show the components of the particle's self-induced velocity disturbance obtained by subtracting the undisturbed velocity from the filtered velocity solution to Eqs. (119) and (120). They also show the projection of the particle's trajectory in the (x, y) plane up until the time at which the snapshot is taken. The right columns show the particle's self-induced velocity disturbance reconstructed with the proposed model of Eq. (72). They also show the stream of transient Stokeslet sources that are advected by the background flow, colored by their time of injection relative to the current snapshot time. Qualitative differences between the velocity disturbance observed in the simulation and that estimated with the proposed model are hardly perceivable, indicating that an accurate recovery of the undisturbed velocity from the filtered flow is possible even in this highly transient case with significant inertial effects.

A quantitative analysis of the proposed model is shown in Figures 18, 19, and 20. Similarly to the previous case of a fixed particle, Figure 18 displays the normalized velocity disturbance interpolated to the center of the particle at $\text{Re}_n = 0.01$ and for $d_n/\Delta x \in \{\frac{1}{8}, \frac{1}{4}, \frac{1}{2}, 1, 2, 4\}$. In the left column is plotted the norm of the difference between the undisturbed velocity, $\tilde{\mathbf{u}}$, and the filtered velocity, $\bar{\mathbf{u}}$, interpolated to the particle center. It is then normalized by the maximum magnitude of the relative velocity between the particle and the undisturbed flow. In the right column, this value is corrected by further subtracting the velocity disturbance modeled by Eq. (72). The left and right plots therefore display the relative errors that would be made in the estimation of the fluid force acting on the particle when not using our model (left) and when using it (right). Figure 19 displays the same normalized velocity disturbance interpolated to the center of the particle for $d_n/\Delta x = 4$ and at $\text{Re}_n \in \{\frac{1}{100}, \frac{1}{10}, 1, 10, 100\}$. Finally, Figure 20 summarizes this study by showing the maximum error made with/without correction across the tested parameter space. Without correction, i.e., by interpolating the filtered velocity at the particle location to estimate drag, a maximum normalized error of about 75% can be made, similarly to the case of a fixed particle. When using our proposed model to correct this interpolated filtered velocity, the maximum normalized error that is made is reduced to about 13%. This demonstrates that the proposed model is not only able to accurately reconstruct the particle's self-induced velocity disturbance for a particle with constant velocity, but also in highly transient and inertia dominated environments.

6.3. Particle settling under the influence of gravity

We now consider the case of an isolated particle settling under the influence of gravity in a very large domain filled with quiescent fluid (i.e., the undisturbed velocity for this particle is $\tilde{\mathbf{u}} = \mathbf{0}$). We only consider the steady drag force and the gravitational force acting on the particle. In such a case, Newton's second law, Eq. (6), becomes

$$\frac{d\mathbf{U}_n(t)}{dt} = -\frac{\mathbf{U}_n(t)}{\tau_n} + \mathbf{g}, \quad (132)$$

where τ_n is the particle time-scale given as

$$\tau_n = \frac{\rho_n d_n^2}{18\mu f(\text{Re}_n)}, \quad (133)$$

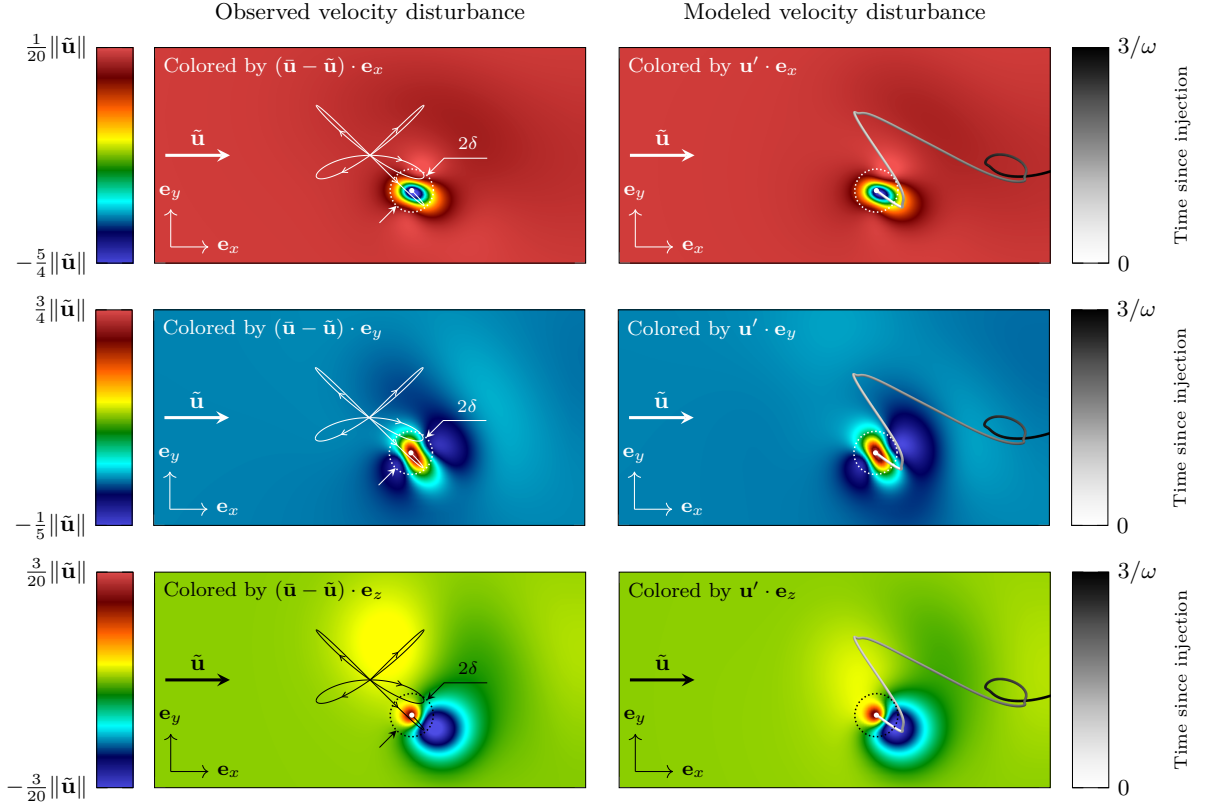


Figure 16: Snapshots of the volume-filtered simulation of a particle oscillating with a prescribed trajectory in a uniform flow with constant far-field velocity $\bar{\mathbf{u}}$ at the Reynolds number $\text{Re}_n = d_n \|\bar{\mathbf{u}}\| / \nu = 1$. The Wendland filter \mathcal{W} defined in Eq. (A.11) is used with $\delta = 2d_n$ and with the resolution $d_n / \Delta x = 4$. These snapshots are taken at a simulation time $t \simeq 11/3\omega$. The left column shows the particle’s self-induced velocity disturbance obtained by subtracting the undisturbed flow velocity $\tilde{\mathbf{u}}$ from the filtered velocity $\bar{\mathbf{u}}$ solution to the volume-filtered governing equations. The right column shows the reconstruction of the particle’s self-induced velocity disturbance with the model proposed in Eq. (72). It also displays the stream of “Stokeslet sources” advected by the background flow and used by the model, which are colored in a gray scale according to the difference between the current time and their time of injection. The rows correspond, from top to bottom, to the x -, y -, and z -components of the velocity disturbance.

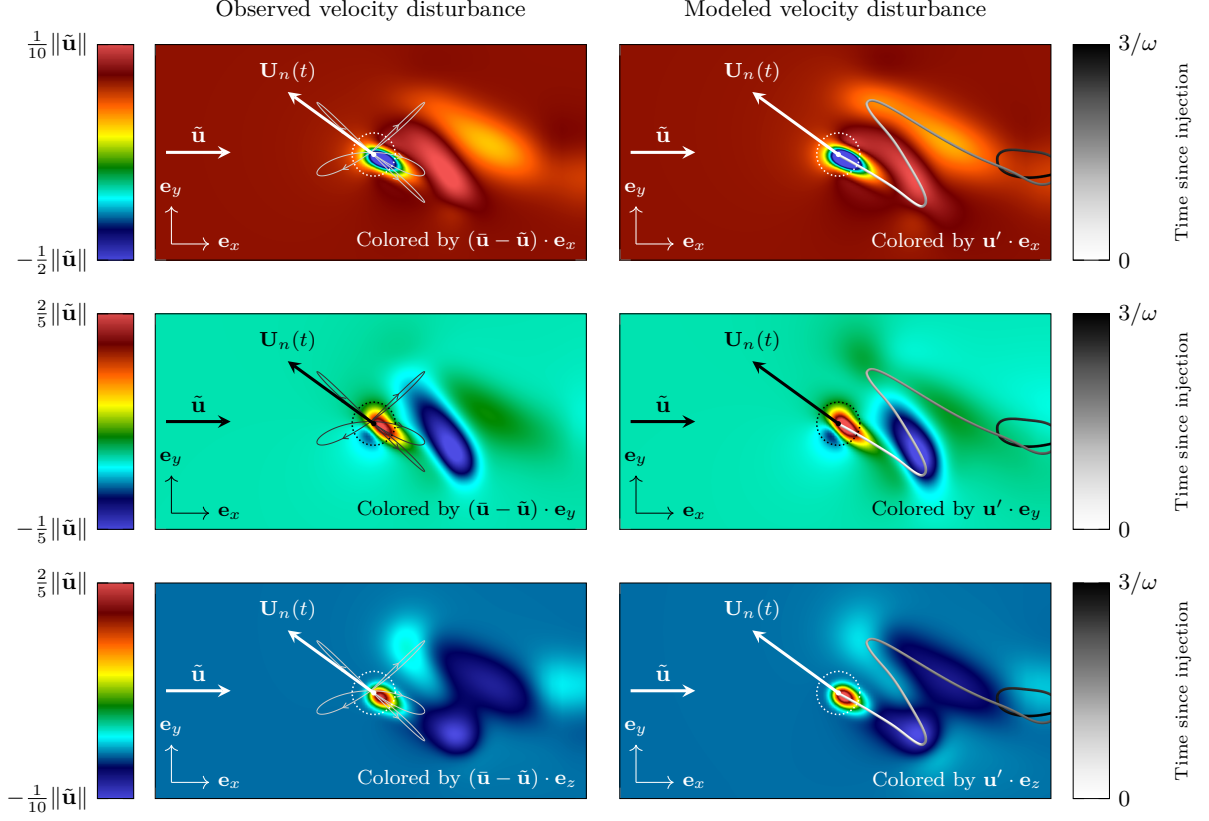


Figure 17: Snapshots of the volume-filtered simulation of a particle oscillating with a prescribed trajectory in a uniform flow with constant far-field velocity $\tilde{\mathbf{u}}$ at the Reynolds number $\text{Re}_n = d_n \|\tilde{\mathbf{u}}\| / \nu = 10$. The Wendland filter \mathcal{W} defined in Eq. (A.11) is used with $\delta = 2d_n$ and with the resolution $d_n / \Delta x = 4$. These snapshots are taken at a simulation time $t \simeq 4/\omega$. The left column shows the particle’s self-induced velocity disturbance obtained by subtracting the undisturbed flow velocity $\tilde{\mathbf{u}}$ from the filtered velocity $\tilde{\mathbf{u}}$ solution to the volume-filtered governing equations. The right column shows the reconstruction of the particle’s self-induced velocity disturbance with the model proposed in Eq. (72). It also displays the stream of “Stokeslet sources” advected by the background flow and used by the model, which are colored in a gray scale according to the difference between the current time and their time of injection. The rows correspond, from top to bottom, to the x -, y -, and z -components of the velocity disturbance.

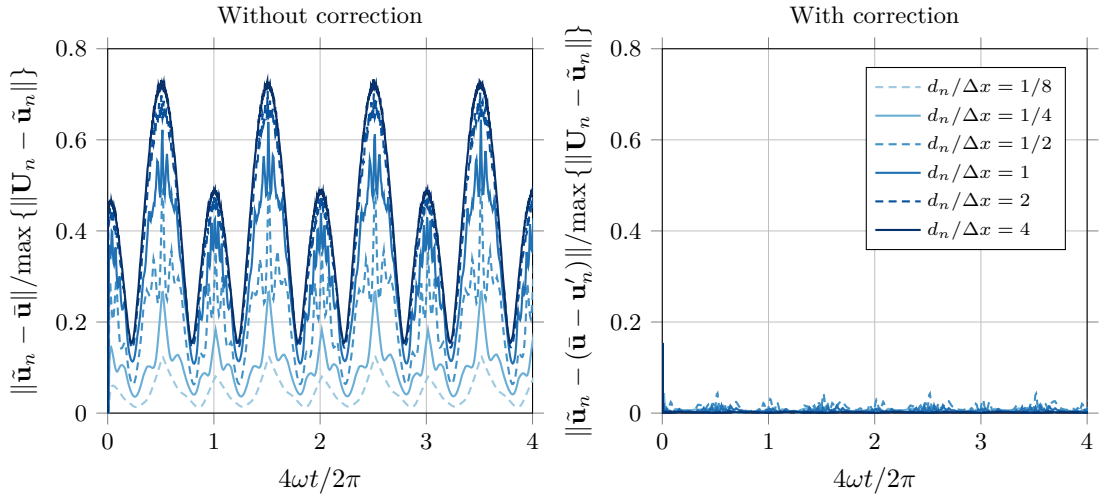


Figure 18: Error made in the estimation of the undisturbed velocity at the location of the oscillating particle without (left) and with (right) the proposed modeled correction (using Eq. (72)), normalized by the maximum relative velocity between the particle and undisturbed flow. In this figure, the Reynolds number is fixed to $\text{Re}_n = 0.01$ while $d_n / \Delta x$ is varied in $\{\frac{1}{8}, \frac{1}{4}, \frac{1}{2}, 1, 2, 4\}$. Four periods of oscillation of the particle are considered.

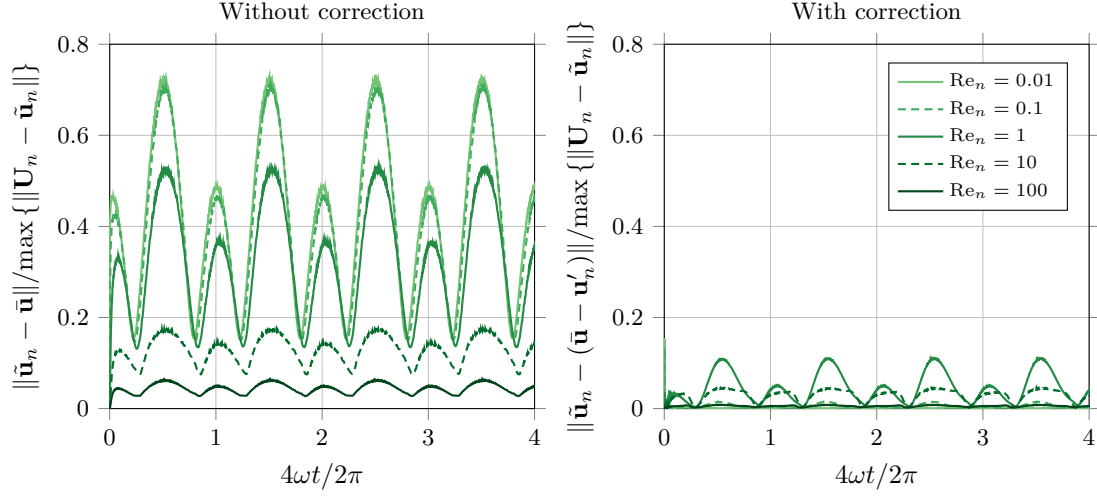


Figure 19: Error made in the estimation of the undisturbed velocity at the location of the oscillating particle without (left) and with (right) the proposed modeled correction (using Eq. (72)), normalized by the maximum relative velocity between the particle and undisturbed flow. In this figure, the resolution is fixed to $d_n/\Delta x = 4$ while the Reynolds number is varied in $\{\frac{1}{100}, \frac{1}{10}, 1, 10, 100\}$. Four periods of oscillation of the particle are considered.

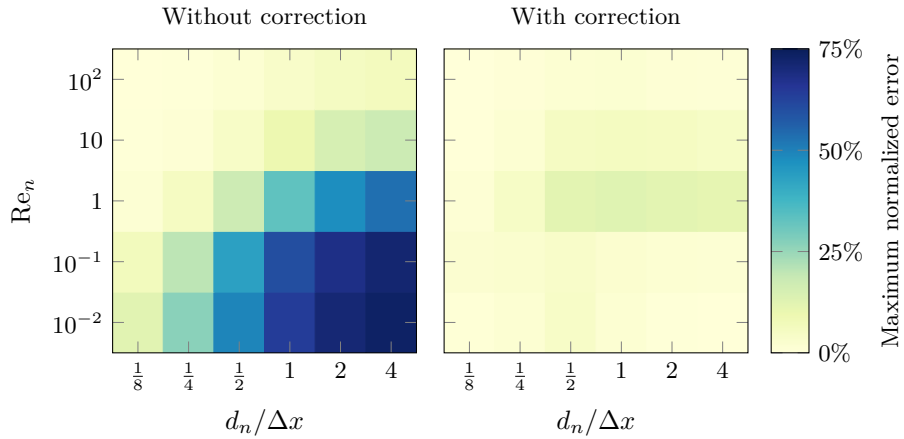


Figure 20: Maximum error made in the estimation of the undisturbed velocity at the location of the fixed particle without (left) and with (right) the proposed modeled correction (using Eq. (72)), normalized by the maximum relative velocity between the particle and undisturbed flow. The values are taken inside one period of oscillation of the particle.

and with Re_n the Reynolds number of the particle defined as

$$\text{Re}_n = \frac{d_n \|\mathbf{U}_n(t)\|}{\nu}. \quad (134)$$

Note that $f(\text{Re}_n)$ is again the Schiller and Naumann [10] empirical correction factor given in Eq. (123). The terminal velocity reached by the particle is given by

$$\mathbf{U}_{n,\infty} = \lim_{t \rightarrow \infty} \mathbf{U}_n(t) = \tau_n \mathbf{g}. \quad (135)$$

This case has been studied in the vast majority of papers that propose models for recovering the undisturbed velocity in volume-averaged Euler-Lagrange simulations [e.g., 6, 27, 31]. In order to quantify the influence of transient effects in the development of the particle’s self-induced flow disturbance, we introduce a Stokes number based on the viscous time-scale of the regularization/filtering kernel, τ_ν , defined in Eq. (93). This Stokes number reads as

$$\text{St}_n = \frac{\tau_n}{\tau_\nu} = \frac{\rho_n d_n^2}{18 \rho \ell^2 f(\text{Re}_n)}. \quad (136)$$

When $\text{St}_n \ll 1$, the rate at which the particle’s self-induced flow disturbance develops is slower than the rate at which the particle relaxes to its terminal velocity. Therefore, one should expect that it is critical for a model recovering the undisturbed velocity to account for transient effects, so as to accurately predict the time evolution of the particle. When $\text{St}_n \gg 1$, on the other hand, one should expect steady models as proposed in [6, 31] to be sufficient for accurately predicting the evolution of the particle.

Figure 21 displays the predicted settling velocity of the particle normalized by its terminal velocity. The Wendland kernel \mathcal{W} defined in Eq. (A.11) is used to regularize the momentum exchange term \mathbf{f} in Eqs. (119) and (120). The radius of the kernel’s support is chosen equal to two particle diameters, $\delta = 2d_n$, and the resolution $d_n/\Delta x = 2$ is employed in the vicinity of the particle. This corresponds to 8 cells across the filter’s support. The flow solver timestep is chosen as $\Delta t = \min(\tau_\nu/2, \tau_n/20, \Delta x/2 \|\mathbf{U}_{n,\infty}\|)$. The Reynolds number of the particle based on its terminal velocity is set to $\text{Re}_n = 0.1$. Each row of Figure 21 corresponds to a Stokes number $\text{St}_n \in \{0.2, 2, 20\}$. Each column of Figure 21 corresponds to a choice of operator for interpolating the fluid velocity at the location of the particle. In the left column, tri-linear interpolation is used. In the right column, the regularization kernel \mathcal{W} is used as interpolation kernel, as proposed in [31]. In each plot of Figure 21, we report four results:

1. The “exact” velocity of the settling particle, predicted using the exact undisturbed velocity $\tilde{\mathbf{u}} = \mathbf{0}$.
2. The velocity of the settling particle obtained when no correction is employed, i.e., the filtered fluid velocity $\bar{\mathbf{u}}$, solution to Eqs. (119) and (120), is used to approximate the undisturbed velocity $\tilde{\mathbf{u}}$.
3. The velocity of the settling particle obtained when a steady correction is employed to approximate the undisturbed velocity $\tilde{\mathbf{u}}$: With tri-linear interpolation, the steady correction of Evrard et al. [16] is used; With the interpolation kernel \mathcal{W} , the steady correction of Evrard et al. [31] is used.
4. The velocity of the settling particle obtained when the model of Eq. (72) is used to approximate the particle’s self-induced velocity disturbance for recovering the undisturbed velocity $\tilde{\mathbf{u}}$.

From Figure 21, one can observe that the accuracy of a steady correction model such as proposed in [6, 16, 31] improves with increasing Stokes number (as defined per Eq. (136)). As expected, as well, applying no correction to the interpolated filtered fluid velocity leads to a large overestimation of the particle’s terminal velocity. Finally, for all Stokes numbers considered, the proposed transient model works as intended and approximates the transient evolution of the particle’s self induced velocity disturbance with high accuracy. This leads to a near-exact prediction of the particle’s terminal velocity, but also of the evolution of its velocity over time.

To provide some illustrative context, a sand particle of diameter $d_n = 0.1$ mm sedimenting in water would display, at terminal velocity, a Reynolds number $\text{Re}_n = \mathcal{O}(1)$ and a Stokes number $\text{St}_n = \mathcal{O}(0.1)$ according to the definitions of Eqs. (134) and (136). These conditions are close to those of the bottom row of Figure 21, in which no correction led to a significant overestimation of the particle’s terminal velocity, while a steady correction led to its significant underestimation. Hence, the use of a transient model such as the one proposed in Eq. (72) for approximating the particle’s self-induced velocity disturbance may radically improve the accuracy of the simulation of particle-laden flows with such physical parameters.

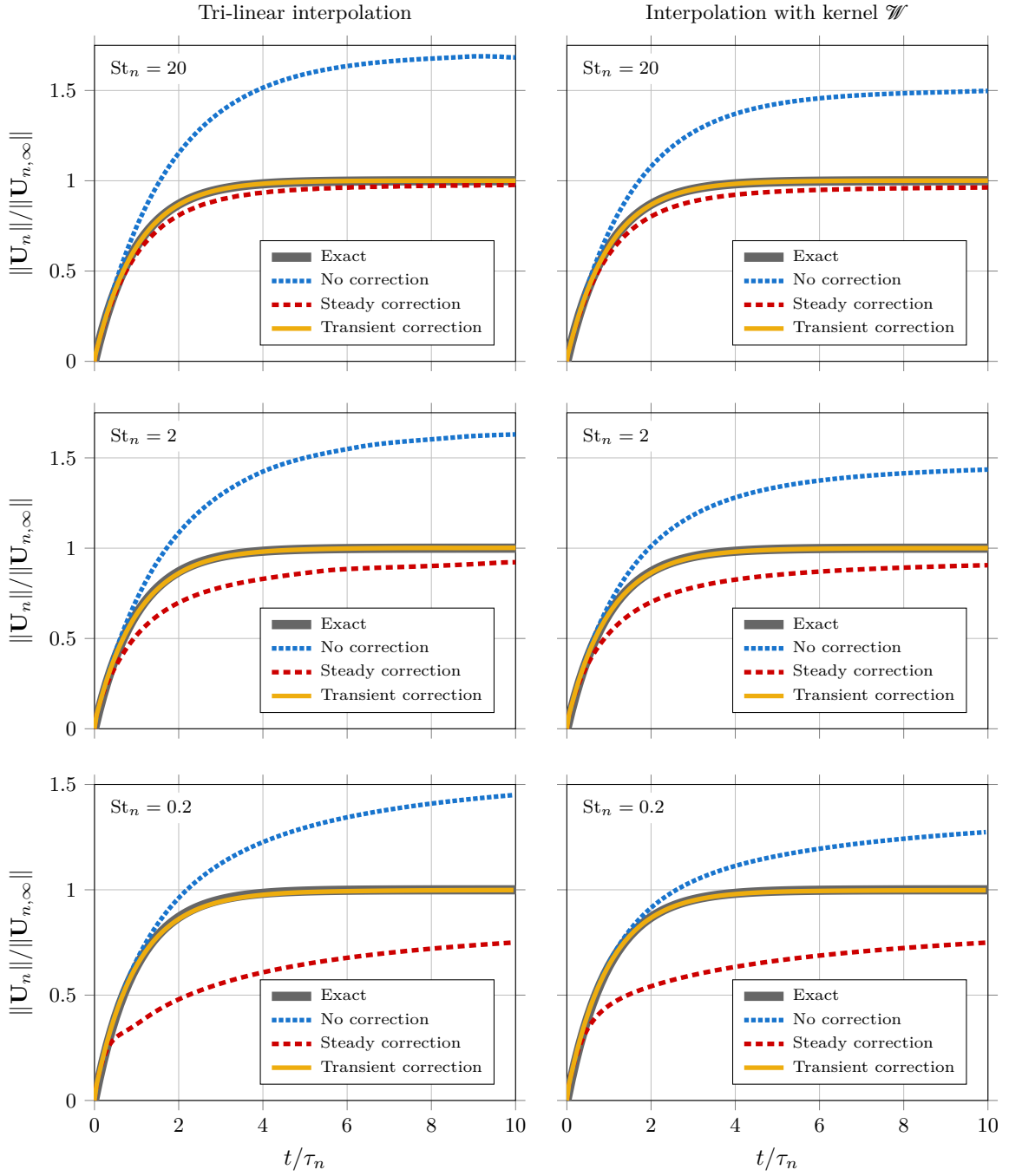


Figure 21: Velocity of a particle settling under the influence of gravity in the VF-EL framework, normalized by its terminal velocity. The Reynolds number of the particle, based on its terminal velocity, is $Re_n = 0.1$. From top to bottom, the Stokes number of the particle, based on the viscous time-scale of the filtering kernel, is $St_n \in \{20, 2, 0.2\}$. In the left column, velocity is interpolated at the particle location using tri-linear interpolation. In the right column, the filtering kernel is used as interpolation kernel too. Each plot reports the exact expected particle velocity, the particle velocity when no correction is applied to the interpolated filtered velocity, the particle velocity when the steady corrections of Evrard et al. [16] and Evrard et al. [31] are applied to the interpolated filtered velocity, and the particle velocity when the model of Eq.(72) is used to correct the filtered velocity.

6.4. Truncation of the forcing history

We have shown in Section 5.1 that the contribution of the m^{th} previous forcing instance in the discrete time-convolution of Eq. (72) decays proportional to $m^{-2/3}$. This means that the sum in Eq. (72) may be truncated without significantly affecting the accuracy of the model. We provide in Figure 5 an estimation of the relative importance of the m^{th} previous forcing instance relative to the most recent one, for a regularization with the Gaussian kernel and for a range of values of the ratio $\Delta t/\tau_\nu$.

In this section, we consider the previously described case of settling particle with $Re_n = 0.1$ and $St_n = 20$, and gradually decrease the threshold beyond which previous forcing instances are discarded in the estimation the particle’s self-induced velocity disturbance. To be more precise, the terms of Eq. (72) for which $t - t^{(k)} > \Upsilon$ are dropped in the estimation of \mathbf{u}' . We consider the limits $\Upsilon \in \{\infty, 100, 50, 25, 12.5, 6.25\} \times \tau_\nu$. Note that for this specific case, the particle time-scale is 20 times the filter’s viscous time-scale, $\tau_n = 20\tau_\nu$.

Figure 22, compares the particle velocity predicted using the truncated transient model correction to the exact particle velocity. As expected, reducing Υ – which amounts to reducing the amount of terms considered in the sum of Eq. (72) – leads to an error in the estimation of the particle’s self-induced velocity disturbance. In the extreme case we have considered, for which $\Upsilon = 6.25\tau_\nu$, only 12 previous forcing instances are stored for estimating the particle’s self-induced velocity disturbance with Eq. (72). In this case, the particle’s terminal velocity is predicted with an error of about 10% while no correction at all leads to an error of about 75%.

Overall, the choice of truncating the forcing history of a given particle for estimating its self-induced velocity disturbance is one that balances the level of accuracy one wishes to reach with the computational costs one can afford. Truncating the sum in Eq. (72) will reduce the computational cost and memory footprint of the model, but may results in undisturbed velocity predictions that are significantly erroneous. A transient correction model that considers as few as one or two previous forcing instances is better than no correction at all, and is relatively cheap. However, for certain flow configurations, it may not perform as well as the steady correction models previously proposed in the literature [e.g., 6, 31], which bear computational costs of a similar order of magnitude as one or two transient correction contributions.

7. Conclusions

This manuscript proposes a new model for recovering the undisturbed velocity associated with a particle in volume-filtered Euler-Lagrange simulations of particle-laden flows. This model is built upon the linearization of the equations governing the flow perturbation induced by a particle, whose solution can then be written in the form of a temporal and spatial convolution integral involving known analytical operators. These convolution integrals are discretized with first-order accuracy in time and second-order accuracy in space. The resulting approximate solution of the particle’s self-induced velocity disturbance is a linear combination of regularized transient Stokeslet contributions, and does not rely on any ad hoc or empirical parameter. The model accounts for the transient development of the velocity disturbance, is shown to provide accurate estimations at finite particle Reynolds numbers, and does not require the momentum feedback force and the particle’s relative velocity vector to be aligned, enabling the consideration of fluid forces other than the steady drag force.

The proposed model is first tested on VF-EL cases of particles with prescribed motion. These tests consider particle Reynolds numbers spanning four orders of magnitude, and mesh resolutions ranging from 1 cell (PSI-CELL equivalent) to 16 cells across the filter support. Over these 60 test-cases, some of which display significant transient and inertial effects in the development of the particle’s self-induced flow disturbance, the proposed model consistently enables the recovery of the undisturbed velocity with a relative error on the order of a few percents. A maximum relative error of about 13% is obtained with the proposed model, whereas an error of up to 75% can be reached without any correction. The model is then tested on cases of particles settling under the influence of gravity, varying the Stokes number defined with respect to the viscous time-scale of the filter. The proposed model then consistently outperforms a steady correction model, and enables high-accuracy prediction of the particle’s velocity.

The high degree of accuracy of the proposed model comes at the cost of seeding and keeping track of fluid tracers along the trajectory of each particle. In order to keep the associated computational cost low, the discrete time convolution sum of Eq. (72) can be truncated. The choice of a threshold beyond which such truncation is applied is one that must balance available computational resources with the desired accuracy. It is also one that depends on the specificities of the case under consideration, especially on the ratio of the solver timestep over the viscous time-scale of the filter.

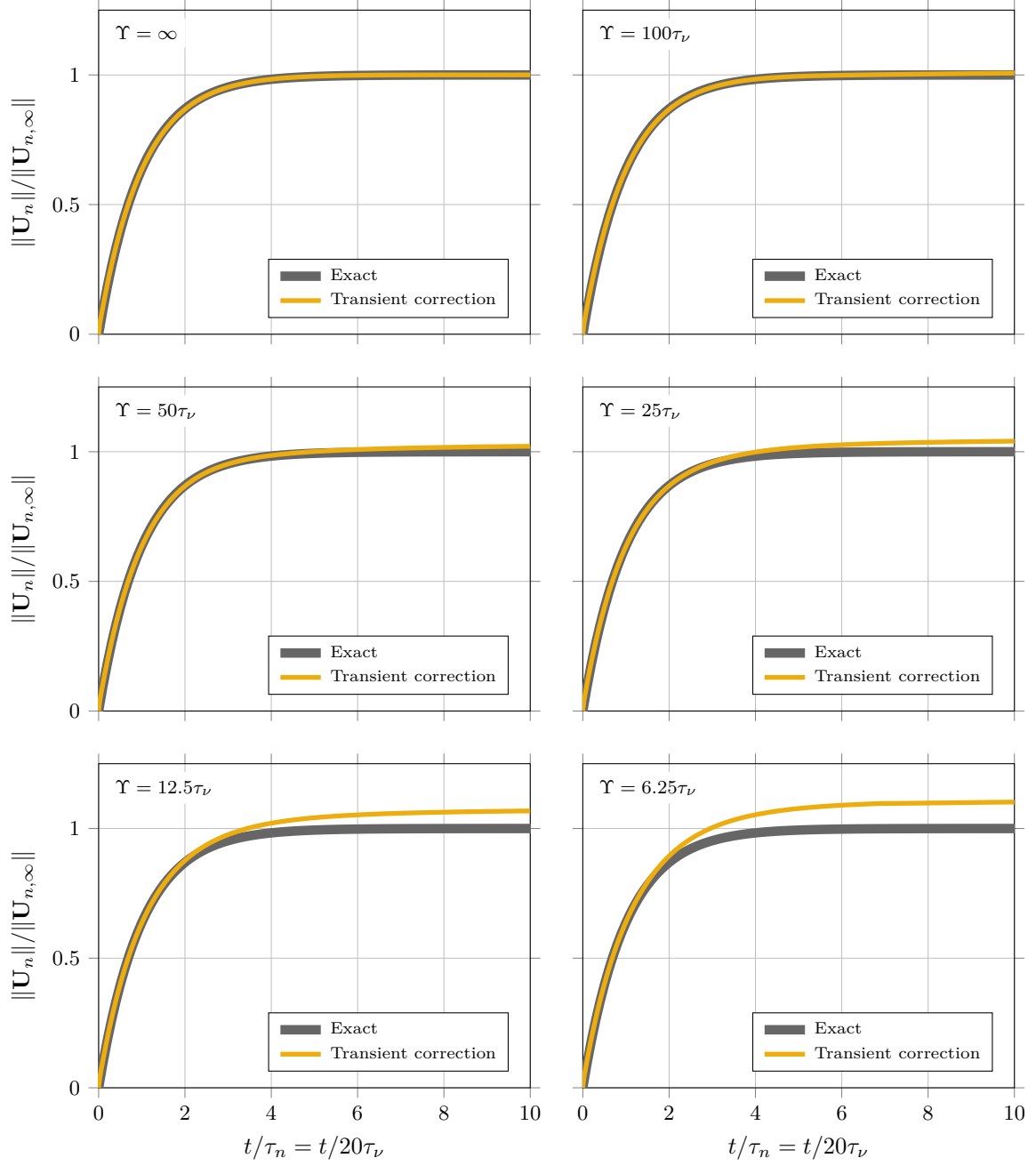


Figure 22: Velocity of a particle settling under the influence of gravity in the VF-EL framework, normalized by its terminal velocity. The Reynolds number of the particle, based on its terminal velocity, is $Re_n = 0.1$ and its Stokes number of the particle, based on the viscous time-scale of the filtering kernel, is $St_n = 20$. Velocity is interpolated to the particle location using tri-linear interpolation. From top left to bottom right, the threshold beyond which previous forcing instances are discarded in the estimation the velocity disturbance is gradually decreased, from $\Upsilon = \infty$ to $\Upsilon = 6.25\tau_\nu$. The particle velocity obtained using the (truncated) model of Eq. (72) to correct the filtered velocity is compared against the exact expected particle velocity.

Appendix A. Closed-form expressions of some regularized transient Stokeslet operators

Appendix A.1. Top-hat filter

Consider the top-hat radial filter kernel

$$\mathcal{H}(r) = \frac{3}{4\pi\delta^3} \begin{cases} 1 & r < \delta \\ 0 & r \geq \delta \end{cases}. \quad (\text{A.1})$$

At $\mathbf{x} = \mathbf{0}$, the convolution of the transient persistent Stokeslet tensor operator with \mathcal{H} yields the diagonal operator

$$\mathcal{S}_{\mathcal{H}}(\mathbf{0}, t) = \mathcal{I} \mathcal{S}_{\mathcal{H}_0}(t), \quad (\text{A.2})$$

where $\mathcal{S}_{\mathcal{H}_0}$ is defined as in Eq. (89),

$$\mathcal{S}_{\mathcal{H}_0}(t) = \frac{4\pi}{\mu} \frac{3}{4\pi\delta^3} \int_0^\delta \left(r^2 \mathcal{H}_1(r, t) + \frac{r^4}{3} \mathcal{H}_2(r, t) \right) dr. \quad (\text{A.3})$$

This reads as

$$\mathcal{S}_{\mathcal{H}_0}(t) = \frac{1}{4\pi\delta\mu} \left(1 - \left(1 - \frac{2\nu t}{\delta^2} \right) \operatorname{erf} \left(\frac{\delta}{\sqrt{4\nu t}} \right) - \frac{2}{\delta} \sqrt{\frac{\nu t}{\pi}} \exp \left(-\frac{\delta^2}{4\nu t} \right) \right). \quad (\text{A.4})$$

The corresponding quantity for the steady regularized Stokeslet is given as

$$\lim_{t \rightarrow \infty} \mathcal{S}_{\mathcal{H}_0}(t) = \frac{1}{4\pi\delta\mu}. \quad (\text{A.5})$$

Note that this steady solution corresponds to the solution derived by Evrard et al. [16] in the limit of vanishing Reynolds number.

Appendix A.2. Gaussian filter

Consider the gaussian filter kernel

$$\mathcal{G}(r) = \frac{1}{(2\pi\sigma^2)^{3/2}} \exp \left(\frac{-r^2}{2\sigma^2} \right). \quad (\text{A.6})$$

At $\mathbf{x} = \mathbf{0}$, the convolution of the transient persistent Stokeslet tensor operator with \mathcal{G} yields the diagonal operator

$$\mathcal{S}_{\mathcal{G}}(\mathbf{0}, t) = \mathcal{I} \mathcal{S}_{\mathcal{G}_0}(t), \quad (\text{A.7})$$

where $\mathcal{S}_{\mathcal{G}_0}$ is defined as in Eq. (89),

$$\mathcal{S}_{\mathcal{G}_0}(t) = \frac{4\pi}{\mu} \frac{1}{(2\pi\sigma^2)^{3/2}} \int_0^\infty \exp \left(\frac{-r^2}{2\sigma^2} \right) \left(r^2 \mathcal{H}_1(r, t) + \frac{r^4}{3} \mathcal{H}_2(r, t) \right) dr. \quad (\text{A.8})$$

This reads as

$$\mathcal{S}_{\mathcal{G}_0}(t) = \frac{1}{3\pi\sqrt{2\pi}\sigma\mu} \left(1 - \frac{\sigma}{\sqrt{2\nu t + \sigma^2}} \right). \quad (\text{A.9})$$

The corresponding quantity for the steady regularized Stokeslet is given as

$$\lim_{t \rightarrow \infty} \mathcal{S}_{\mathcal{G}_0}(t) = \frac{1}{3\pi\sqrt{2\pi}\sigma\mu}. \quad (\text{A.10})$$

Note that this steady solution was derived by Balachandar et al. [6].

Appendix A.3. Wendland filter

Consider the compactly supported, polynomial Wendland filter kernel [30]

$$\mathcal{W}(r) = \frac{21}{2\pi\delta^3} \begin{cases} \left(\frac{4r}{\delta} + 1\right) \left(1 - \frac{r}{\delta}\right)^4 & r < \delta \\ 0 & r \geq \delta \end{cases}. \quad (\text{A.11})$$

At $\mathbf{x} = \mathbf{0}$, the convolution of the transient persistent Stokeslet tensor operator with \mathcal{W} yields the diagonal operator

$$\mathcal{S}_{\mathcal{W}}(\mathbf{0}, t) = \mathcal{I} \mathcal{S}_{\mathcal{W}}(t), \quad (\text{A.12})$$

where $\mathcal{S}_{\mathcal{W}_0}$ is defined as in Eq. (89),

$$\mathcal{S}_{\mathcal{W}_0}(t) = \frac{4\pi}{\mu} \frac{21}{2\pi\delta^3} \int_0^\delta \left(\frac{4r}{\delta} + 1\right) \left(1 - \frac{r}{\delta}\right)^4 \left(r^2 \mathcal{H}_1(r, t) + \frac{r^4}{3} \mathcal{H}_2(r, t)\right) dr. \quad (\text{A.13})$$

This reads as

$$\begin{aligned} \mathcal{S}_{\mathcal{W}_0}(t) = \frac{1}{2\pi\delta\mu} & \left(1 + \sqrt{\frac{\nu t}{\pi}} (3584\delta^{-5}\nu^2 t^2 + 6144\delta^{-7}\nu^3 t^3) \right. \\ & - (1 - 14\delta^{-2}\nu t + 420\delta^{-4}\nu^2 t^2 + 4200\delta^{-6}\nu^3 t^3) \operatorname{erf}\left(\frac{\delta}{\sqrt{4\nu t}}\right) \\ & \left. - \frac{2}{\delta} \sqrt{\frac{\nu t}{\pi}} (1 - 16\delta^{-2}\nu t + 460\delta^{-4}\nu^2 t^2 + 3072\delta^{-6}\nu^3 t^3) \exp\left(-\frac{\delta^2}{4\nu t}\right) \right). \end{aligned} \quad (\text{A.14})$$

The corresponding quantity for the steady regularized Stokeslet is given as

$$\lim_{t \rightarrow \infty} \mathcal{S}_{\mathcal{W}_0}(t) = \frac{1}{2\pi\delta\mu}. \quad (\text{A.15})$$

Note that this steady solution was derived by Evrard et al. [31].

Acknowledgements

This work has been funded by the Deutsche Forschungsgemeinschaft (DFG), grant number 457515061. The authors are grateful to Olivier Desjardins for providing guidance and resources that have supported the work presented in this manuscript. The authors are also grateful to the National Center for Supercomputing Applications (NCSA) at the University of Illinois Urbana-Champaign for providing access to HPC resources for the current work. Finally, the authors thank Sivaramakrishnan Balachandar and Jesse Capecelatro for enlightening and constructive discussions on the topic of undisturbed velocity recovery over the years.

References

- [1] T. B. Anderson, R. Jackson, Fluid Mechanical Description of Fluidized Beds. Equations of Motion, Industrial & Engineering Chemistry Fundamentals 6 (1967) 527–539.
- [2] M. Ishii, T. Hibiki, Thermo-Fluid Dynamics of Two-Phase Flow, Springer US, Boston, MA, 2006.
- [3] S. Balachandar, J. K. Eaton, Turbulent Dispersed Multiphase Flow, Annual Review of Fluid Mechanics 42 (2010) 111–133.
- [4] P. Peipot, O. Desjardins, Numerical analysis of the dynamics of two- and three-dimensional fluidized bed reactors using an Euler–Lagrange approach, Powder Technology 220 (2012) 104–121.
- [5] J. Capecelatro, O. Desjardins, An Euler–Lagrange strategy for simulating particle-laden flows, Journal of Computational Physics 238 (2013) 1–31.
- [6] S. Balachandar, K. Liu, M. Lakhote, Self-induced velocity correction for improved drag estimation in Euler–Lagrange point-particle simulations, Journal of Computational Physics 376 (2019) 160–185.
- [7] S. Elghobashi, On predicting particle-laden turbulent flows, Applied Scientific Research 52 (1994) 309–329.
- [8] M. R. Maxey, J. J. Riley, Equation of motion for a small rigid sphere in a nonuniform flow, The Physics of Fluids 26 (1983) 883–889.
- [9] R. Gatignol, The Faxén formulas for a rigid particle in an unsteady non-uniform Stokes-flow, Journal de Mécanique Théorique et Appliquée 2 (1983) 143–160.

- [10] L. Schiller, A. Naumann, Über die grundlegenden Berechnungen bei der Schwerkraftaufbereitung, *Zeitschrift des Vereines Deutscher Ingenieure* 77 (1933) 318–320.
- [11] R. Clift, W. H. Gauvin, Motion of entrained particles in gas streams, *The Canadian Journal of Chemical Engineering* 49 (1971) 439–448.
- [12] R. Clift, J. R. Grace, M. E. Weber, *Bubbles, Drops, and Particles*, Dover Publ, Mineola, NY, nachdr. der ausg. new york, ny acad. press, 1978 edition, 2013.
- [13] P. G. Saffman, The lift on a small sphere in a slow shear flow, *Journal of Fluid Mechanics* 22 (1965) 385–400.
- [14] M. Boivin, O. Simonin, K. D. Squires, Direct numerical simulation of turbulence modulation by particles in isotropic turbulence, *Journal of Fluid Mechanics* 375 (1998) 235–263.
- [15] S. Balachandar, A scaling analysis for point-particle approaches to turbulent multiphase flows, *International Journal of Multiphase Flow* 35 (2009) 801–810.
- [16] F. Evrard, F. Denner, B. van Wachem, Quantifying the errors of the particle-source-in-cell Euler-Lagrange method, *International Journal of Multiphase Flow* 135 (2021) 103535.
- [17] C. T. Crowe, M. P. Sharma, D. E. Stock, The Particle-Source-In Cell (PSI-CELL) Model for Gas-Droplet Flows, *Journal of Fluids Engineering* 99 (1977) 325–332.
- [18] J.-F. Poustis, J.-M. Senoner, D. Zuzio, P. Villedieu, Regularization of the Lagrangian point force approximation for deterministic discrete particle simulations, *International Journal of Multiphase Flow* 117 (2019) 138–152.
- [19] F. Evrard, F. Denner, B. van Wachem, A hybrid Eulerian-Lagrangian approach for simulating liquid sprays, in: 29th Conference on Liquid Atomization and Spray Systems, Paris.
- [20] Y. Pan, S. Banerjee, Numerical simulation of particle interactions with wall turbulence, *Physics of Fluids* 8 (1996) 2733–2755.
- [21] M. Maxey, B. Patel, Localized force representations for particles sedimenting in Stokes flow, *International Journal of Multiphase Flow* 27 (2001) 1603–1626.
- [22] S. Lomholt, M. R. Maxey, Force-coupling method for particulate two-phase flow: Stokes flow, *Journal of Computational Physics* 184 (2003) 381–405.
- [23] P. Gualtieri, F. Picano, G. Sardina, C. M. Casciola, Exact regularized point particle method for multiphase flows in the two-way coupling regime, *Journal of Fluid Mechanics* 773 (2015) 520–561.
- [24] F. Battista, J.-P. Mollicone, P. Gualtieri, R. Messina, C. M. Casciola, Exact regularised point particle (ERPP) method for particle-laden wall-bounded flows in the two-way coupling regime, *Journal of Fluid Mechanics* 878 (2019) 420–444.
- [25] J. Horwitz, A. Mani, Accurate calculation of Stokes drag for point-particle tracking in two-way coupled flows, *Journal of Computational Physics* 318 (2016) 85–109.
- [26] J. Horwitz, A. Mani, Correction scheme for point-particle models applied to a nonlinear drag law in simulations of particle-fluid interaction, *International Journal of Multiphase Flow* 101 (2018) 74–84.
- [27] P. J. Ireland, O. Desjardins, Improving particle drag predictions in Euler–Lagrange simulations with two-way coupling, *Journal of Computational Physics* 338 (2017) 405–430.
- [28] M. Esmaily, J. Horwitz, A correction scheme for two-way coupled point-particle simulations on anisotropic grids, *Journal of Computational Physics* 375 (2018) 960–982.
- [29] P. Pakseresht, M. Esmaily, S. V. Apte, A correction scheme for wall-bounded two-way coupled point-particle simulations, *Journal of Computational Physics* 420 (2020) 109711.
- [30] H. Wendland, Piecewise polynomial, positive definite and compactly supported radial functions of minimal degree, *Advances in Computational Mathematics* 4 (1995) 389–396.
- [31] F. Evrard, F. Denner, B. van Wachem, Euler-Lagrange modelling of dilute particle-laden flows with arbitrary particle-size to mesh-spacing ratio, *Journal of Computational Physics: X* 8 (2020) 100078.
- [32] S. Balachandar, K. Liu, A correction procedure for self-induced velocity of a finite-sized particle in two-way coupled Euler–Lagrange simulations, *International Journal of Multiphase Flow* 159 (2023) 104316.
- [33] P. Pakseresht, S. V. Apte, A disturbance corrected point-particle approach for two-way coupled particle-laden flows on arbitrary shaped grids, *Journal of Computational Physics* 439 (2021) 110381.
- [34] J. Horwitz, G. Iaccarino, J. Eaton, A. Mani, The discrete Green’s function paradigm for two-way coupled Euler–Lagrange simulation, *Journal of Fluid Mechanics* 931 (2022) A3.
- [35] J. Kim, S. Balachandar, Finite volume fraction effect on self-induced velocity in two-way coupled Euler-Lagrange simulations, *Physical Review Fluids* 9 (2024) 034306.
- [36] V. Chéron, F. Evrard, B. van Wachem, A hybrid immersed boundary method for dense particle-laden flows, *Computers & Fluids* 259 (2023) 105892.
- [37] M. Uhlmann, A. Chouippe, Clustering and preferential concentration of finite-size particles in forced homogeneous-isotropic turbulence, *Journal of Fluid Mechanics* 812 (2017) 991–1023.
- [38] L. Schneiders, M. Meinke, W. Schröder, Direct particle–fluid simulation of Kolmogorov-length-scale size particles in decaying isotropic turbulence, *Journal of Fluid Mechanics* 819 (2017) 188–227.
- [39] L. Schneiders, K. Fröhlich, M. Meinke, W. Schröder, The decay of isotropic turbulence carrying non-spherical finite-size particles, *Journal of Fluid Mechanics* 875 (2019) 520–542.
- [40] D. A. Drew, *Mathematical Modeling of Two-Phase Flow*, *Annual Review of Fluid Mechanics* 15 (1983) 261–291.
- [41] M. Hausmann, V. Chéron, F. Evrard, B. van Wachem, Study and derivation of closures in the volume-filtered framework for particle-laden flows (2024).
- [42] H. Faxén, Der Widerstand gegen die Bewegung einer starren Kugel in einer zähen Flüssigkeit, die zwischen zwei parallelen ebenen Wänden eingeschlossen ist, *Annalen der Physik* 373 (1922) 89–119.
- [43] C. Pozrikidis, *Introduction to Theoretical and Computational Fluid Dynamics*, Oxford University Press, New York, 2nd ed edition, 2011.
- [44] A. T. Chan, A. T. Chwang, The unsteady stokeslet and oseenlet, *Proceedings of the Institution of Mechanical Engineers, Part C: Journal of Mechanical Engineering Science* 214 (2000) 175–179.
- [45] R. Cortez, The Method of Regularized Stokeslets, *SIAM Journal on Scientific Computing* 23 (2001) 1204–1225.
- [46] F. Denner, F. Evrard, B. van Wachem, Conservative finite-volume framework and pressure-based algorithm for flows of incompressible, ideal-gas and real-gas fluids at all speeds, *Journal of Computational Physics* 409 (2020) 109348.